Energetics of Surface Melt in West Antarctica

Madison L. Ghiz[1], Ryan C. Scott[2], Andrew M. Vogelmann[3], Jan T. M. Lenaerts[4], Matthew Lazzara[5], Dan Lubin[1]

[1]Scripps Institution of Oceanography, University of California San Diego, La Jolla CA 92093-0206 USA
[2]NASA Langley Research Center, Hampton VA 23666 USA
[3]Environmental and Climate Sciences Department, Brookhaven National Laboratory, Upton NY 11973-5000 USA
[4]Department of Atmospheric and Oceanic Sciences, University of Colorado, Boulder CO 80309-0311 USA
[5]Antarctic Meteorological Research Center, SSEC, University of Wisconsin, Madison WI 53706 USA

Correspondence to: Dan Lubin (dlubin@ucsd.edu)

Abstract. We use reanalysis data and satellite remote sensing of cloud properties to examine how meteorological conditions alter the surface energy balance to cause surface melt that is detectable in satellite passive microwave imagery over West Antarctica. This analysis can detect each of the three primary mechanisms for inducing surface melt at a specific location: thermal blanketing involving sensible heat flux and/or longwave heating by optically thick cloud cover, all-wave radiative enhancement by optically thin cloud cover, and föhn winds. We examine case studies over Pine Island and Thwaites Glaciers, which are of interest for ice shelf and ice sheet stability, and over Siple Dome, which is more readily accessible for field work. During January 2015 over Siple Dome we identified a melt event whose origin is an all-wave radiative enhancement by optically thin clouds. During December 2011 over Pine Island and Thwaites Glaciers, we identified a melt event caused mainly by thermal blanketing from optically thick clouds. Over Siple Dome, those same 2011 synoptic conditions yielded a thermal blanketing-driven melt event that was initiated by an impulse of sensible heat flux then prolonged by cloud longwave heating. In contrast, a late-summer thermal blanketing period over Pine Island and Thwaites Glaciers during February 2013 showed surface melt initiated by cloud longwave heating then prolonged by enhanced sensible heat flux. At a location on the Ross Ice Shelf adjacent to the Transantarctic mountains we identified a December 2011 föhn wind case with additional support from automatic weather station data. One limitation thus far with this type of analysis involves uncertainties in the cloud optical properties. Nevertheless, with improvements this type of analysis can enable quantitative prediction of atmospheric stress on the vulnerable Antarctic ice shelves in a steadily warming climate.

1 Introduction

The contribution of West Antarctic mass loss to sea level rise, presently the second largest cryospheric contribution to sea level rise after the Greenland Ice Sheet (Mouginot et al., 2019; Rignot et al., 2019), is driven by a complex mechanical and thermodynamic system involving grounded ice sheets, their floating ice shelf extensions, and the surrounding ocean and atmosphere. While a warming ocean causes a retreat of West Antarctic ice sheet grounding lines on numerous reverse slopes, by gradually accelerating the ice sheet outflow via the well-known marine ice sheet instability (MISI; Weertman, 1974;

Oppenheimer, 1998; Joughin et al., 2014; Alley et al., 2015), the ice shelves mitigate this outflow through the buttressing they provide by being in contact with adjacent land masses (Fürst et al., 2016). But the ice shelves are themselves thinning via basal melting from the warming ocean (Pritchard et al., 2012; Paolo et al., 2015), which compromises their buttressing strength and

35 also enhances the overall meltwater loss of Antarctic glacial ice (Adusumilli et al., 2020). Structural integrity of an ice shelf can be further compromised when surface meltwater filters through crevasses into its interior mass, rendering the extremities more vulnerable to wave action (DeConto and Pollard, 2016; Bell et al., 2018). Extensive summer melt ponds occurring in a warming atmosphere were the major factor in the loss of the Larsen B Ice Shelf in 2002 (Scambos et al., 2003; van den Broeke, 2005; Glasser and Scambos, 2008). The loss of this ice shelf immediately facilitated faster ice calving of the upstream glaciers

40 (Scambos et al., 2004). In 2008 similar ice shelf failures occurred on the Wilkins Ice Shelf, at the base of the Antarctic Peninsula near West Antarctica proper (Scambos et al., 2009). Surface and lower tropospheric warming are now understood to prevail throughout West Antarctica and across the Ross Ice Shelf (RIS) as far as Ross Island (Steig et al., 2009; Bromwich et al., 2013).

45 Remote sensing studies now document frequent warm-season surface melting over West Antarctica and the Ross Ice Shelf (e.g., Kingslake et al., 2017). The energetics of a major melt event over West Antarctica during January 2016 were measured with modern atmospheric science equipment during the joint US Antarctic Program and Department of Energy Atmospheric Radiation Measurement (ARM) user facility's West Antarctic Radiation Experiment (AWARE; Nicolas et al., 2017; Lubin et al., 2020). These measurements provided insight into the role of atmospheric thermodynamics and cloud radiative properties

50 in generating local surface melt. But in contrast to the Antarctic Peninsula and Greenland Ice Sheet, West Antarctic melt events tend to be shorter in duration and exhibit greater spatial, interannual and intra-seasonal variability. Remote sensing assessment of their total meltwater equivalent (e.g., Kuipers Munneke et al., 2012), which is much smaller than that of basal melting, can give the impression that surface melt might not be an important consideration. But the potential for West Antarctic surface melt to aggravate ice mass loss involves structural degradation of ice shelves through ponding and hydrofracturing, as has

55 already happened throughout much of the Antarctic Peninsula region. Recent studies of Antarctic ice mass balance now account for spatial and temporal variability on multiple scales (Lenaerts et al., 2018; Donat-Magnin et al., 2020; Adusumilli et al., 2020). When evaluating the potential impact of surface melt in West Antarctica, one should focus on assessing the frequency and duration of melt events directly on the vulnerable ice shelves, and also on determining the specific physical mechanisms causing each melt event.

60

Over the cryosphere the surface energy balance (SEB) can be expressed in terms of the melt energy ME (W m^{-2}):

$$ME = F_{SW}^{\downarrow} - F_{SW}^{\uparrow} + F_{LW}^{\downarrow} - F_{LW}^{\uparrow} + F_{SH} + F_{LH} - G \qquad (1)$$

65   where the individual energy components are the downwelling and upwelling shortwave (SW) and longwave (LW) radiation, the sensible heat flux (SH), the latent heat flux (LH) and the ground conduction G. The sum of the four SW and LW fluxes is the net radiation. The sum of SH and LH fluxes is the net turbulent flux, and here we use the European Centre for Medium-Range Weather Forecasts (ECMWF) convention where a positive sign signifies energy going into the surface. Over Antarctic firn G is usually very small on daily timescales compared to the radiative and turbulent fluxes (e.g., Fisher et al. 2015), though

70   it can become somewhat important on sub-daily timescales (i.e., warming of the snowpack in the morning, and cooling it at night, after potential refreezing). Advection of air warmer than 0°C appears in the ME as positive SH flux, whose magnitude depends on both the air temperature gradient and the wind speed. Strictly speaking equation (1) is valid when the snow surface temperature T_s is at or above the melt point. If T_s is below the melt point and the SEB doesn't close, it is likely due to ground conduction. Local radiative heating of a snowpack can induce melt at temperatures as low as -2°C by internal scattering and

75   absorption (e.g., Nicolas et al., 2017). If T_s is at or above freezing a positive ME maintains surface melting while a negative ME represents a surface cooling that if sustained will reduce the surface temperature below freezing. A negative ME also represents a phase change (i.e., refreezing of the surface, if the T_s is at the melt point. The actual cooling happens through LW radiation and ground conduction.

80   If the ME remains positive across at least two diurnal cycles, then this condition combined with skin or 2-m air temperatures at or just below freezing is often associated with a surface melt that is detectable in satellite passive microwave (PMW) data (Nicolas et al., 2017). This does not mean that surface melt is occurring throughout those diurnal cycles. Melt occurs only when T_s is between -2°C and 0°C, depending on surface microphysics. And the PMW data are instantaneous observations made twice daily (morning and evening overpasses). At colder T_s, the positive ME goes into warming the snowpack but does not

85   cause detectable melt. Identification of an episodes in the ME time series that remains positive across two or more diurnal cycles should therefore be regarded as a strong indicator of satellite-detectable melt at some point during the episode.

    The largest individual terms in (1) are the upwelling and downwelling radiative fluxes, and they are strongly modulated by cloud cover which is extensive over West Antarctica (Scott et al., 2017). Therefore the net (downwelling minus upwelling)

90   radiative fluxes are just as capable of driving $ME > 0$ for extended time periods as a strong impulse of positive SH flux. The result is that three distinct mechanisms for inducing surface melt can be at play over West Antarctic ice sheets, either individually or in conjunction reinforcing each other.

    One mechanism is thermal blanketing. If an airmass contains overcast cloud cover within a few hundred meters of the surface

95   having liquid water path (LWP) > 50 gm^{-2}, this cloud cover will radiate in the LW as a blackbody at very close to surface temperature, while also attenuating the net SW flux. The result is a surface net LW flux close to zero, and sometimes even positive, along with a constantly positive net SW flux that has a diurnal cycle of relatively small amplitude. If the net turbulent flux is also positive such that the ME remains positive over two more diurnal cycles, this will usually induce surface melt, if

the starting skin temperature is warm enough (e.g., Trusel et al., 2013). This situation prevailed during the large-scale January

100   2016 melt event over West Antarctica (Nicolas et al., 2017). Wille et al. (2019) have correlated most Antarctic surface melt
events with the presence of atmospheric rivers (ARs). If ARs impinging on the Antarctic continent tend to bring mainly large
cloud *LWP*, then thermal blanketing would be a widespread source of stress on the ice shelves.

A second mechanism involves an all-wave (SW plus LW) radiative enhancement by optically thin clouds. Bennartz et al.

105   (2013) discovered this cloud radiative effect and showed that is extensive over the GIS during warm summers that drive surface
melt. When overcast or broken cloud cover has *LWP* between 10-40 g m^{-2}, generally very common in polar atmospheres, this
cloud cover will radiate substantially toward the surface in the LW while still allowing large SW fluxes to reach the surface.
In combination with a mostly positive net turbulent flux, these clouds can often prolong a positive *ME* over multiple diurnal
cycles, causing surface melt. Van Tricht et al. (2016) found an additional role for optically thin low cloud cover, in slowing

110   down the refreezing of meltwater.

A third mechanism very common throughout Antarctica is a föhn wind. The föhn effect occurs when an airmass crosses high
terrain such as a mountain range. As the airmass is forced upslope it expands and cools, and the moisture condenses and may
form clouds or precipitation, releasing latent heat. Adiabatic descent on the lee side of the high terrain warms the air even more

115   substantially than the latent heat release and, combined with turbulent mixing upon reaching the lower terrain, brings a large
positive turbulent flux input to the surface. Föhn winds are especially prevalent on the lee side of the Antarctic Peninsula,
causing stress to the Larsen C Ice Shelf (e.g., Elvidge et al., 2015; King et al., 2017; Datta et al., 2019). However, due to widely
varying high terrain over Antarctica, in particular the Transantarctic Mountains, föhn winds can occur anywhere and impact
any ice shelf depending on the prevailing synoptic conditions (e.g., Zhou et al., 2018).

120

The objective of this work is to determine if readily available satellite remote sensing and meteorological reanalysis data can
be used to identify the mechanisms that drive specific Antarctic surface melt events. Scott et al. (2019) identify the large-scale
meteorological drivers of West Antarctic surface melt, and the approach presented here considers their application to specific
locations using available satellite and surface data. If successful, then this approach can be used to assess future risk to the

125   vulnerable West Antarctic ice shelves. For example, if melt events occur frequently under common polar meteorological
phenomena such as optically thin clouds that produce the all-wave radiative enhancement, then the stress on the ice shelves
might be perennially constant. Conversely, if melt events occur mainly under optically thick clouds only associated with strong
ARs (e.g., Wille et al., 2019), then one might expect more of a long-term risk in a warming atmosphere. Ultimately multi-year
assessment of melt event mechanisms would need to be understood in terms of the large-scale meteorological drivers (Scott et

130   al., 2019) to make such a risk assessment. Here we demonstrate with case studies that each of the above three melt-inducing
mechanisms can be identified in satellite and reanalysis data.

2 Data and Methods

2.1 Melt Detection

135 We identify the Antarctic surface melt events with a standard PMW technique using the Defense Meteorological Satellite Program (DMSP) Special Sensor Microwave Imager/Sounder (SSMIS), but with a new NASA-supported Making Earth System Data Records for Use in Research Environments (MEaSUREs) data product archived at the National Snow and Ice Data Center (NSIDC). We use the Equal-Area Scalable-Earth Grid version 2 (EASE-Grid 2.0) Level-2 PMW brightness temperature (T_b) at 19.35 GHz with horizontal polarization (19 GHz-H; K-band) from the evening overpass at 25-km grid spacing (Brodzik et al., 2016, updated 2020). We base our melt detection technique on an algorithm originally proposed by

140 Zwally & Feigles (1994) and subsequently refined and validated by Torinesi et al. (2003) and Tedesco (2009). For a given grid cell, surface melt is detected when the PMW T_b measurement exceeds the prior cold season average by 30 K. The cold season average is constructed by averaging daily T_b measurements from 1 April of the prior year through 31 March of the given year. This average is then repeated twice, each time after removing daily values >30 K above the previous average.

145 This technique is generally used to detect and map surface melt over large areas and on seasonal timescales. Here we examine monthly T_b time series in the three regions depicted in Figure 1. The Pine Island and Thwaites Glacier region presents the greatest concern for West Antarctic Ice Sheet (WAIS) loss. Siple Dome is a site at an intermediate elevation on the WAIS (607 m above sea level) that has a multi-decadal automatic weather station (AWS; Lazzara et al., 2012) record and a US Antarctic Program (USAP) summer field camp that has been used for some field work on the physics of snowmelt (Das and Alley 2005;

150 2008). Siple Dome is considered here because it is accessible by the US Antarctic Program for future field work. In addition to the AWS, the University of Wisconsin Antarctic Meteorological Research Center (AMRC) archives manual surface weather observations from numerous field camps and expeditions, and some of these are available for the first four case studies discussed below, over Pine Island Glacier and Siple Dome.

155 We choose a third location on the Ross Ice Shelf (RIS) near the Transantarctic mountains that contains two AWS, Tom (84.430°S, 171.455°W) and Sabrina 84.248°S, 170.044°W), whose data have suggested the presence of strong föhn winds. Each of the regions depicted in Figure 1 contains between 800-1300 25-km EASE-Grid cells. This gives us an opportunity to examine local-scale spatial variability resulting perhaps from varying topography or differential melting and refreezing frequency across the local domain, in addition to time variation. In the monthly T_b time series, we identify melt events of short

160 duration (<5 days) by comparing the daily mean, median, and range with the prior cold season average and the 30-K melt detection threshold. Short duration melt events provide relatively straightforward case studies in which we can readily identify the changing meteorological conditions and shifts in individual ME components that lead to melt onset and subsequent
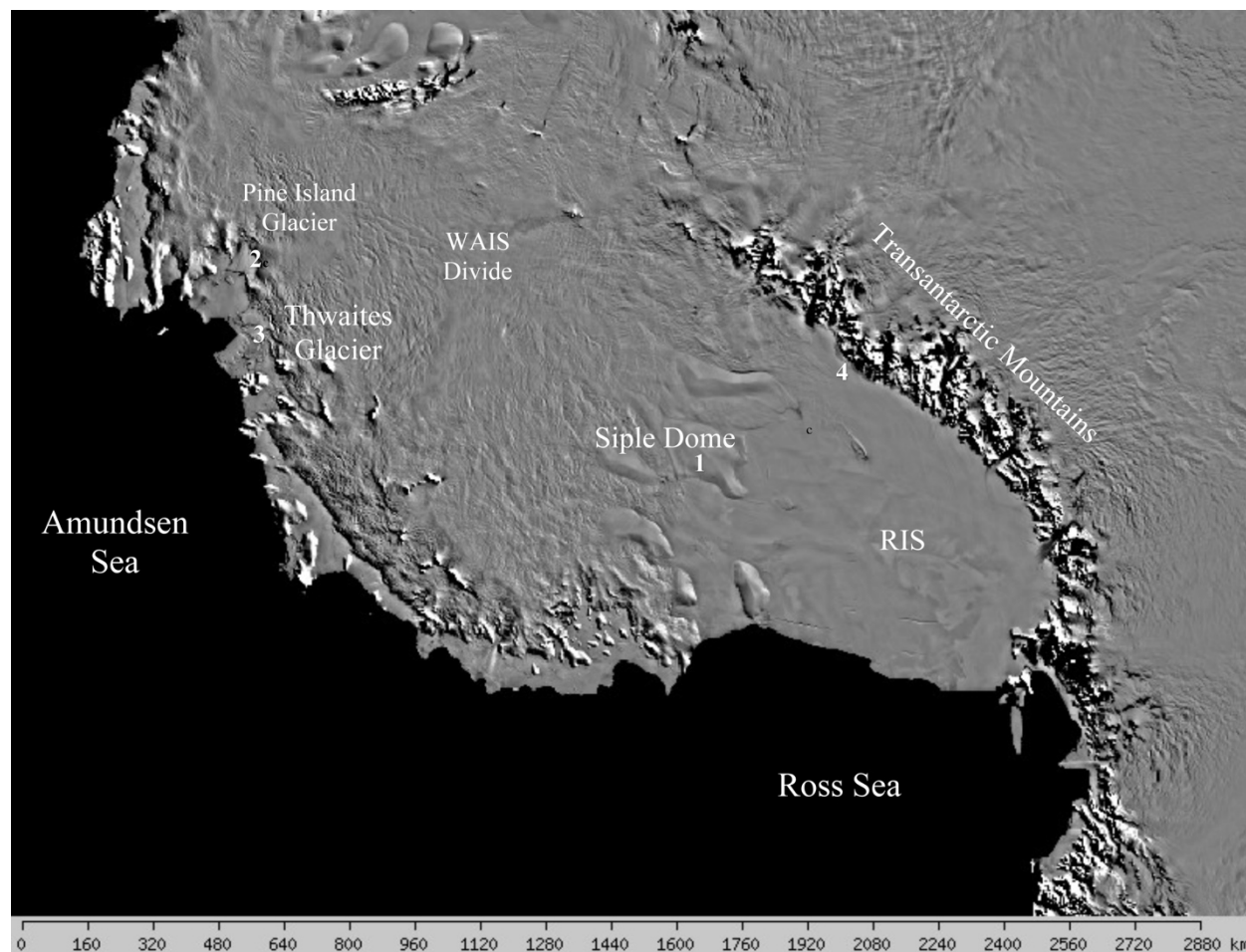
Figure 1. Map of West Antarctica showing the study locations: (1) Siple Dome, (2) Pine Island Glacier, (3) Thwaites Glacier, and (4) RIS location containing the Tom and Sabrina AWS. The AWARE data were collected at the WAIS Divide Ice Camp. Figure constructed from the Mosaic of Antarctica (Scambos et al. 2007; Haran et al., 2014).

recovery. Such case studies allow us to observe the basic physics and develop an understanding of what is driving these surface melt events at a local spatial scale.

2.2 Surface Energy Budget Analysis

For our SEB analysis, we use the fifth-generation ECMWF meteorological reanalysis data (ERA5; Hersbach et al., 2020). Previous studies have shown better agreement between ECMWF data and Antarctic in situ data than other reanalysis models (e.g., Lenaerts et al., 2017). The ERA5 model physics includes prognostic determination of cloud water and ice, cloud fraction, rain and snow (Hersbach et al., 2020), more modern atmospheric radiative transfer schemes than its predecessor ERA-Interim

(Dee et al., 2011), and a sophisticated snow component in the land surface model (Dutra et al. 2010). We compute ME using the surface radiative and turbulent fluxes on a 0.5°x0.5° latitude-longitude grid with hourly time resolution. Other ERA5 fields we analyze include the near-surface (2 m) air temperature, skin temperature, and 850 hPa wind components.

180   However, Silber et al. (2019) compared ERA5 data with AWARE data from the WAIS Divide Ice Camp and found a tendency to overestimate cloud ice water content and underestimate cloud *LWP*. We therefore compare the ERA5 skin temperature, downwelling SW flux and downwelling LW flux with the AWARE measurements at WAIS Divide in Figure 2, to estimate how ERA5 cloud microphysical discrepancies might impact a time series of the ME before and during a melt event. The AWARE flux measurements were made using the ARM user facility pyranometers and pyrgeometers (Mather & Voyles 2013;
185   Lubin et al. 2020). Figure 2a shows that ERA5 consistently underestimates skin temperature except often when the Sun is at its lowest elevation, but that the temperature discrepancy varies from day to day. The instantaneous discrepancies between ERA5 and the measured downwelling SW flux (Figure 2b) can sometimes be on the order of 100 W m^{-2}, but the similarity in amplitudes of the diurnal cycles suggest that ERA5 is reliably simulating the presence of clouds on a daily basis. Much more striking discrepancies appear between ERA5 and measured downwelling LW flux (Figure 2c). Here there are many periods,
190   sometimes a day long, where ERA5 underestimates the LW flux by ~50 W m^{-2}, which would be expected if modeled *LWP* is too low (see Figure 14 in Lubin et al. 2020). There are, however, other periods when the ERA5 and measured LW fluxes are consistent. This episodic nature of the LW flux discrepancies, in which errors can persist throughout a day, suggest that we should find alternative estimates of the cloud *LWP* and ice water path (*IWP*) to evaluate the realism of LW flux calculations in the *ME* based on ERA5 data.

195

We therefore use satellite data products from the NASA Cloud and Earth's Radiant Energy System (CERES) program; specifically, the synoptic 1-degree (SYN1deg) data product. Here CERES top-of-atmosphere (TOA) fluxes, surface fluxes, cloud masking and cloud properties are interpolated to hourly time resolution using geostationary satellite data and gridded to 1° in both latitude and longitude. The SYN1deg product contains NASA A-Train retrievals of cloud *LWP* and *IWP* based
200   primarily on the Moderate-Resolution Imagine Spectroradiometer (MODIS) data from the Aqua spacecraft (Rutan et al., 2015).

Our goal is to be able to evaluate the energetics of surface melt events anywhere in Antarctica, rather than be tied to the few instances such as AWARE where corroborating surface measurements are available. So we examine the contrasts between ERA5 and CERES SYN1deg cloud properties and radiative fluxes during the AWARE January 2016 melt event but at Siple
205   Dome instead of WAIS Divide. From Nicolas et al. (2017) we know that clouds should be optically thick and that the *ME* should be positive over several diurnal cycles after 10 January. Over Siple Dome during the melt, event both ERA5 and CERES indicate *LWP* > 50 g m^{-2} (Figure 3). However, ERA5 cloud *IWP* is sometimes twice as large as the CERES retrieval, and this may reflect the errors discovered by Silber et al. (2019).
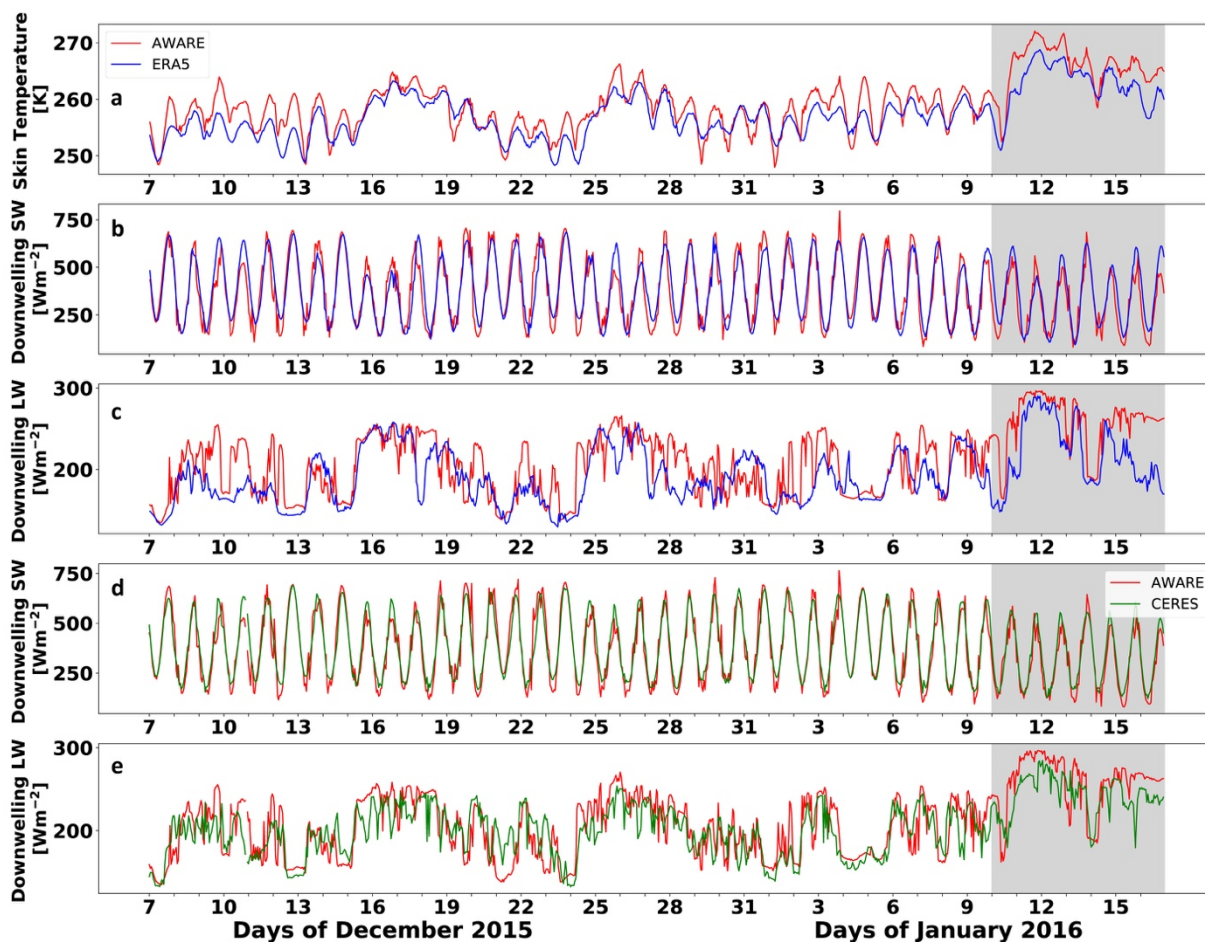
210

Figure 2. Time series comparison of hourly SEB components considered in this work with surface measurements from AWARE (Lubin et al. 2020; red curve in all plots): (a) skin temperature from ERA5; (b) downwelling SW flux from ERA5; (c) downwelling LW flux from ERA5; (d) downwelling SW flux from CERES SYN1deg; (e) downwelling LW flux from CERES SYN1deg. The shaded region indicates the WAIS January 2016 melt event period (Nicolas et al.

215 **2017).**

If cloud microphysics is more realistic in the CERES data product, one might be tempted to calculate the *ME* by replacing ERA5 net radiative fluxes with their CERES counterparts, while retaining the ERA5 turbulent fluxes. We tried this approach for January 2016 over Siple Dome (Figure 4) and the result is unsatisfactory. The diurnal amplitude of the CERES net SW

220 flux is up to twice as large as that modeled by ERA5, and is also qualitatively less consistent with the AWARE measurements from WAIS Divide. There are substantial differences of order 50 W m^{-2} between ERA5 and CERES net LW fluxes, with CERES appearing to be an improvement compared with ERA5's known tendency to underpredict the net LW flux over
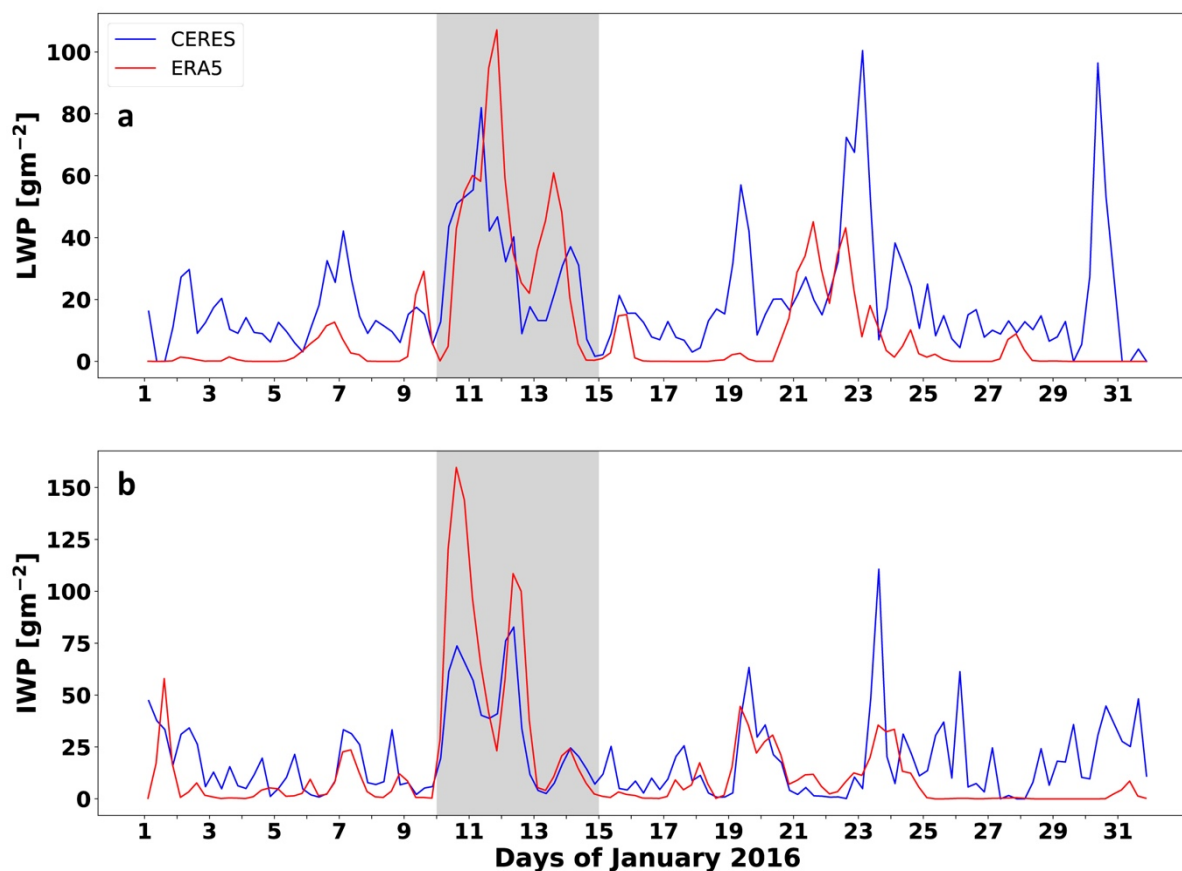
Figure 3. Time series of hourly cloud *LWP* (a) and *IWP* (b) from the CERES SYN1deg data product (red) and ERA5 (blue), over the Siple Dome region throughout January 2016. The shaded region denotes the time period of the WAIS large-scale melt event (Nicolas et al. 2017).

Antarctica. However, the *ME* calculation using ERA5 for all flux terms is basically realistic in that *ME* > 0 over three diurnal cycles after 10 January, and almost always drops below zero at lowest Sun elevation for the rest of the month. When we substitute the CERES radiative fluxes, both the net (SW + LW) radiative flux and *ME* are positive over several diurnal cycles for about half the month, including before 10 January when we know that meteorological conditions were not conducive to surface melt (Nicolas et al., 2017). We therefore conclude that a "mix and match" approach to evaluating the *ME* is unsuitable, and this is not surprising given that ERA5 and CERES use different radiative transfer algorithms. Instead, we proceed by calculating the *ME* with ERA5 radiative and turbulent fluxes, and then examine the CERES SYN1deg cloud *LWP* and *IWP* as a separate check on the realism of cloud properties simulated by ERA5.
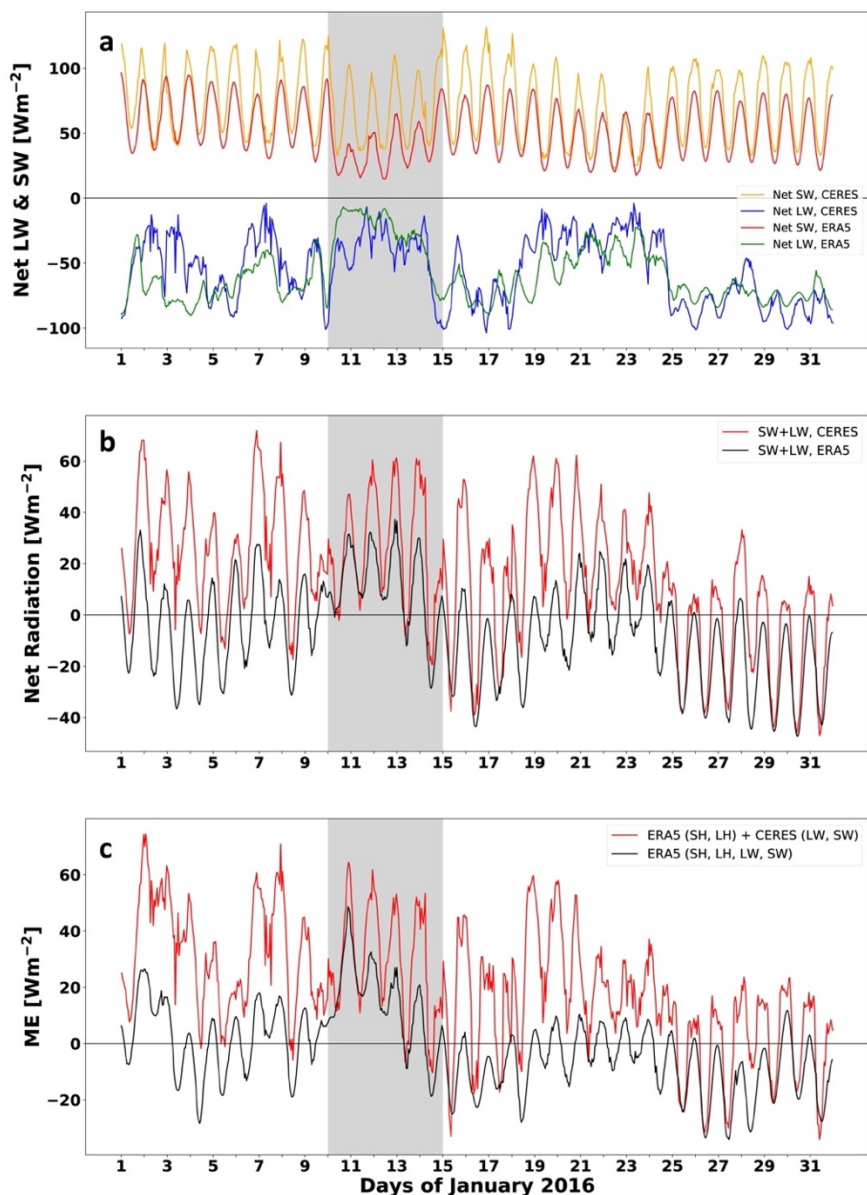
Figure 4. Radiative flux components and alternative estimates of the *ME* over Siple Dome during January 2016: (a) Individual net SW fluxes from ERA5 (red) and CERES SYN1deg data (yellow) and net LW fluxes from ERA5 (green) and CERES SYN1deg data (blue); (b) total net radiative flux from ERA5 (black) and CERES SYN1deg data (red); (c) *ME* computed entirely from ERA5 (black) and using ERA5 turbulent fluxes but substituting the CERES SYN1deg radiative fluxes (red).

3 Results and Discussion

3.1 Siple Dome January 2015

Our first case study shows evidence of an all-wave radiative flux enhancement by optically thin clouds that led to a melt event
245   on Siple Dome between 5-7 January 2015. January 2015 showed a low-pressure system over the Ross-Amundsen Sea that was
blocked briefly by a weak ridge, causing a warm marine airmass to be driven up over the Marie Byrd Land ice cap. The airmass
continued to descend over the Siple Coast. Northerly winds during the event are consistent with strong descent and adiabatic
warming. It is possible that this descent of dry air reduced any potentially optically thick clouds into LWP values within the
Bennartz et al. (2013) thin cloud range.

250

Figure 5a shows the daily T_b statistics throughout the Siple Dome region depicted in Figure 1. The satellite melt, detected using
the 30 K threshold, begins in some of the region on 5 January and extends through most of the region over the next two days.
Figure 5b shows estimates of the surface emissivity sampled from five grid cells with T_b values ranging from the 5th to 99th
percentiles on 6 January. Here surface emissivity is approximated as the ratio of the satellite-measured T_b to the ERA5 skin
255   temperature. Before this short melt event, and also beginning four days after its recovery (after the 12th), the surface emissivity
appears to be spatially uniform. During the melt period the surface shows large variability in emissivity throughout the region,
possibly reflecting differential surface properties resulting from non-uniform snow accumulation or refreezing from prior melt
periods. Similar sampling of the ERA5 radiative and turbulent flux terms (figure not shown) shows much more spatial
uniformity during and outside of the melt period.

260

Figure 6 presents the individual ME components. The shaded region of interest contains the melt onset, peak and partial
recovery. Cloud cover reduces the net SW flux to a monthly minimum on 6 January, while at the same time the net LW flux
rises from < -50 W m^{-2} to ~ -25 W m^{-2} (Figure 6a) The total net radiation is at a monthly maximum on 6 January (Figure 4b).
SH flux is small but mostly positive between 5-9 January (Figure 6c), resulting from warmer air just above the surface but this
265   is largely canceled by mostly negative LH flux so that the net turbulent flux (Figure 6d) does not remain positive over more
than one entire diurnal cycle between 5-9 January. The ME remains positive over two full diurnal cycles 6-7 January (Figure
6e), but at no other time in January. This corresponds with a monthly maximum in 2 m air temperature and skin temperature
(Figure 6f).

270   Cloud LWP and IWP (Figure 7) show discrepancies between ERA5 and CERES SYN1deg, but overall suggest the presence
of optically thin cloud cover. ERA5 predicts very low LWP but an impulse of high IWP on 6 January. This high IWP may be
unrealistic, per Silber et al. (2019). In contrast, CERES data indicate low IWP but an impulse of elevated LWP that briefly
reaches a maximum of 49 g m^{-2} on 6 January. Throughout 5-9 January, the CERES average LWP is 21.2±13.7 g m^{-2}. We note
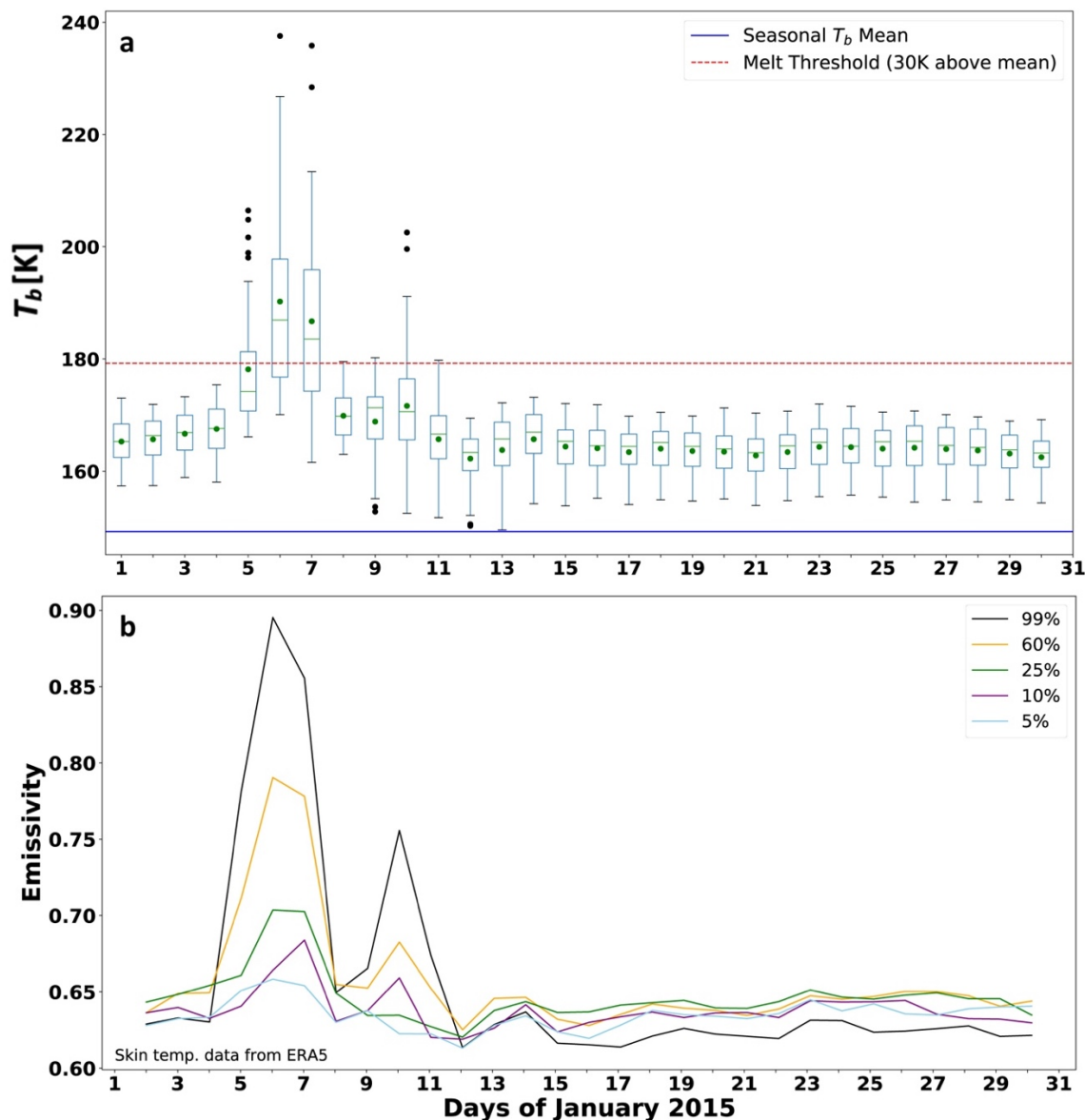
Figure 5. (a) Time series of daily evening overpass SSMIS brightness temperatures T_b over the Siple Dome region during January 2015, as daily statistics with the box denoting the first to third interquartile range (Q_1 to Q_3), the horizontal line in the box denoting the median, the green dot denoting the mean, the whiskers denoting the distance 1.5 ($Q_3 - Q_1$), and individual black points beyond them denoting outliers beyond the range 1.5 ($Q_3 - Q_1$). The blue horizontal line is the prior cold season mean and the red horizontal line is the standard melt detection threshold lying 30 K above the prior cold season mean (Tedesco 2009). (b) Five estimates of surface emissivity sampled throughout the region with percentiles referenced to the maximum T_b value in the region on 6 January.
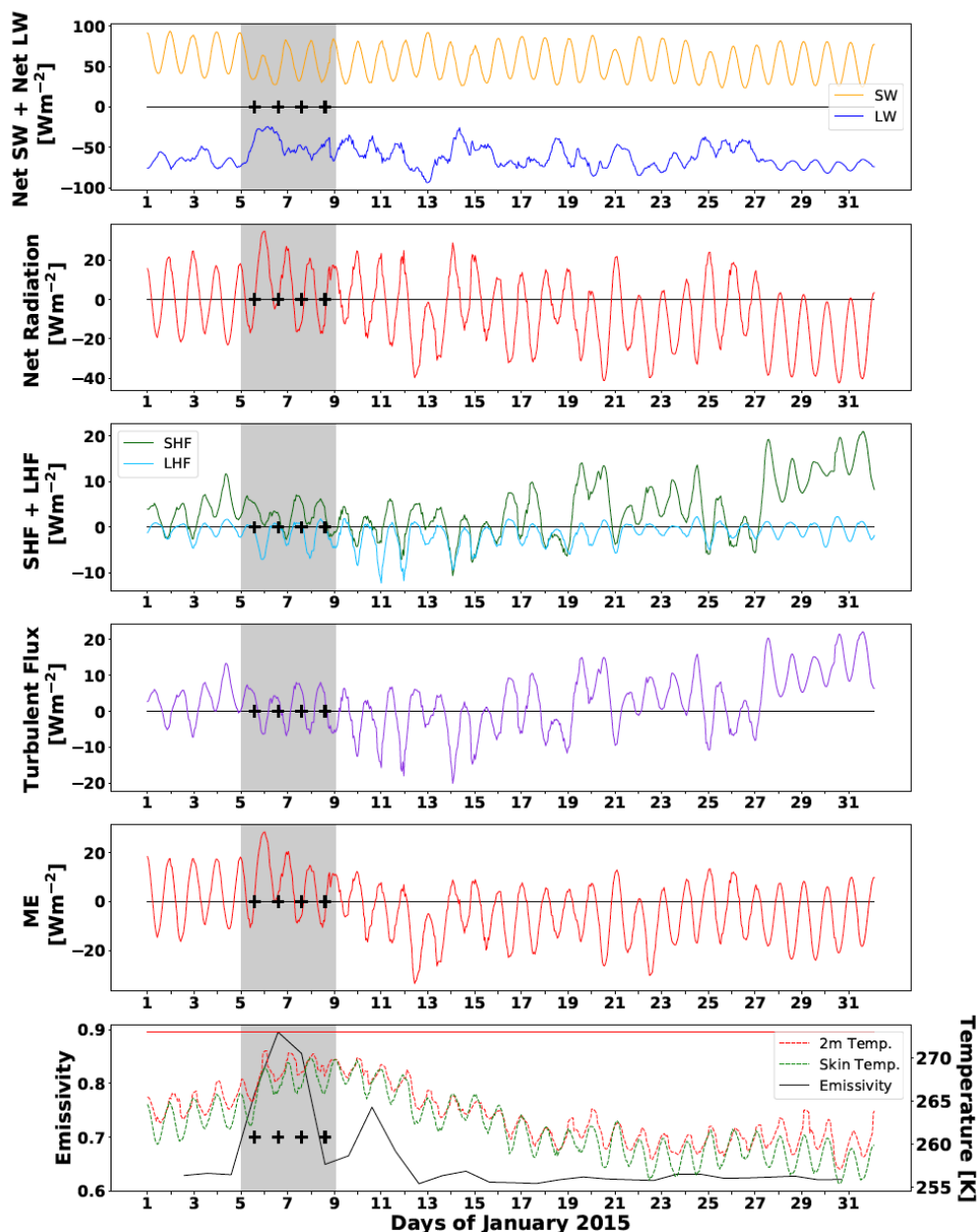
Figure 6. Time series of the hourly *ME* components over the Siple Dome region throughout January 2015 from ERA5: (a) individual net SW and LW fluxes; (b) total net radiative flux (SW + LW); (c) individual SH and LW fluxes; (d) net turbulent flux (SH + LH); (e) total ME; (f) skin temperature (green), 2 m air temperature (red), and sampled 99th percentile emissivity from Figure 3b (black). The horizontal red line in (f) is at 273.15 K. The shaded region denotes the melt period of interest. Black crosses denote the satellite evening overpass times.
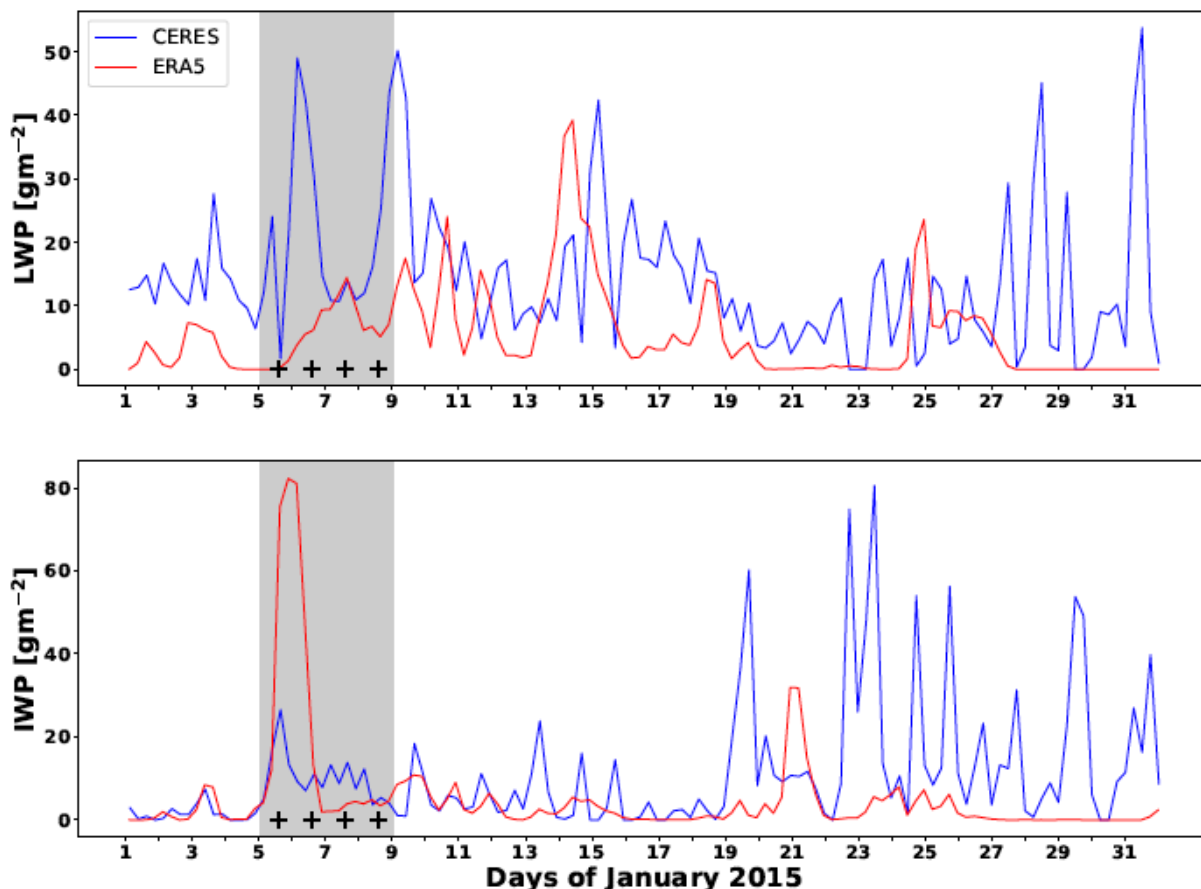
Figure 7. Time series of hourly cloud *LWP* (a) and *IWP* (b) from the CERES SYN1deg data product (red) and ERA5
(blue), over the Siple Dome region throughout January 2015. Black crosses denote the satellite evening overpass times.

that the ERA5 radiative transfer algorithm uses the high *IWP* values when computing the SW and LW fluxes in Figure 6a-b. Examining the vertical profiles in cloud water content over 5-9 January, we find that maximum liquid water content occurs mainly in the pressure range 850-950 hPa, while maximum ice water content occurs in the more vertically extensive pressure range 700-850 hPa (figure not shown). This case study underscores the need for improvement in mixed-phase cloud microphysics used in reanalysis models. We also note that CERES data show a second impulse in cloud *LWP* on 9 January. Being absent in the ERA5 cloud simulation, its effect does not appear in the radiative fluxes in Figure 6a-b. However, it may help to explain the satellite T_b signals of partial surface melt in the region that persist until 11 January (Figure 5). This may be an example of the refreezing inhibition proposed by Van Tricht et al. (2016).

Field camp observations between 5-9 January indicate mostly broken and overcast cloud cover with cloud bases between 900-1800 m and unrestricted visibility, occasionally dropping to ~250 m in reduced visibility with freezing fog or mist and light fog during 8-9 January. On 5-6 January the observer remarks "Sun dimly visible" through the overcast. These observations are qualitatively consistent with optically thin cloud cover.

3.2 Siple Dome December 2011

We now consider two case studies associated with a somewhat deeper warm air and moisture intrusion from the Southern Ocean, first at Siple Dome and then over the Pine Island and Thwaites Glacier region. In December 2011 a deep low-pressure system slowly propagated eastward and drove a warm, moist airmass up over the WAIS. This airmass sat over the WAIS and maintained an optically thick liquid cloud presence over the entire Amundsen Sea Embayment (ASE). This airmass descended and was funneled onto the southern RIS, producing widespread föhn wind effects over that region, including the Siple Coast.

Over Siple Dome this synoptic condition led to several satellite T_b measurements in the > 30-K threshold melt detection range between 22-26 December 2011 (Figure 8). In Figure 8b, we again see spatial uniformity in sampled surface emissivity throughout the prior three weeks; then during the melt period of interest, some surface emissivity values remain low and within the "dry surface" range while others become elevated by as much as 0.16. This is not, however, as pronounced a melt event as that of January 2015 discussed above.

Examining the SEB components, we see that cloud radiative effects (Figure 9a,b) do not substantially alter the SEB until late in the melt period of interest (22-26 December). This melt event instead appears to be induced and dominated by an impulse of SH flux that begins on 19 December (Figure 9c) and causes the net turbulent flux (Figure 9d) and the total ME (Figure 9e) to remain positive through two diurnal cycles before the satellite PMW data show signs of surface melt. During the satellite melt detection period, the ME actually drops below zero at lowest Sun elevations, even as the ERA5 2m air and skin temperatures rise steadily (Figure 9f). Examining the cloud properties (Figure 10), both *LWP* and *IWP* are unexceptional during most of the melt period of interest, compared with the rest of the month, until there is an impulse of moderate to high *LWP* that is simulated by ERA5 two days before a maximum in *LWP* is detected in the CERES MODIS-based remote sensing data. This cloud intrusion having moderate to large optical thickness may help explain the skin and 2m air temperatures between 27-28 December, which are very close together, at or just below freezing, and at monthly maximum values. Overall, this case study suggests a thermal blanketing episode driven primarily by a positive SH flux impulse that began on 19 December, that caused a delayed melt onset as detected by satellite PMW data three days later, and that may have been prolonged by a cloud radiative effect 5-7 days later.
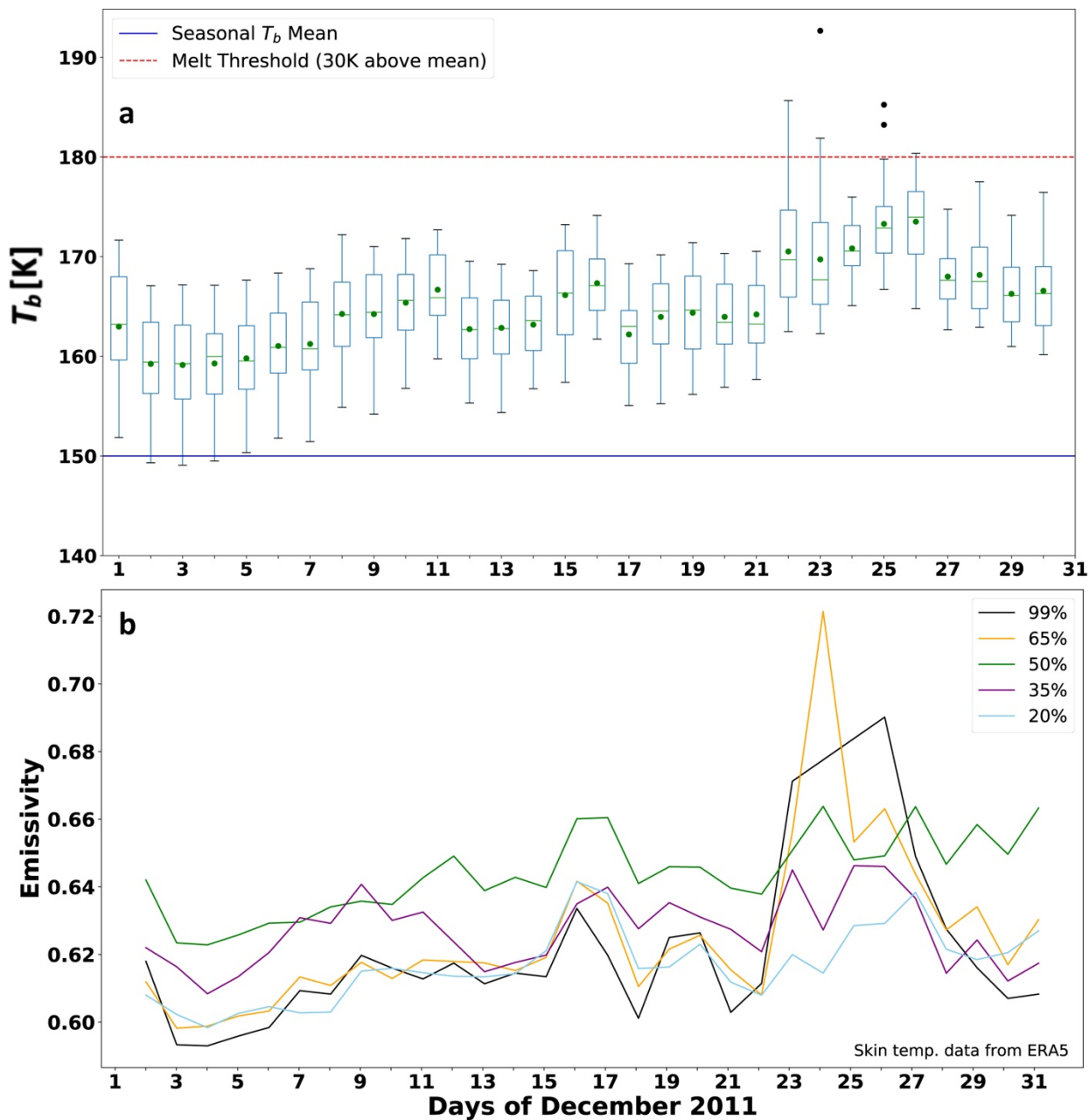
Figure 8. As in Figure 5, but over the Siple Dome region throughout December 2011. The five estimates of surface emissivity in (b) sampled from the region are referenced to the maximum T_b value in the region on 26 December.
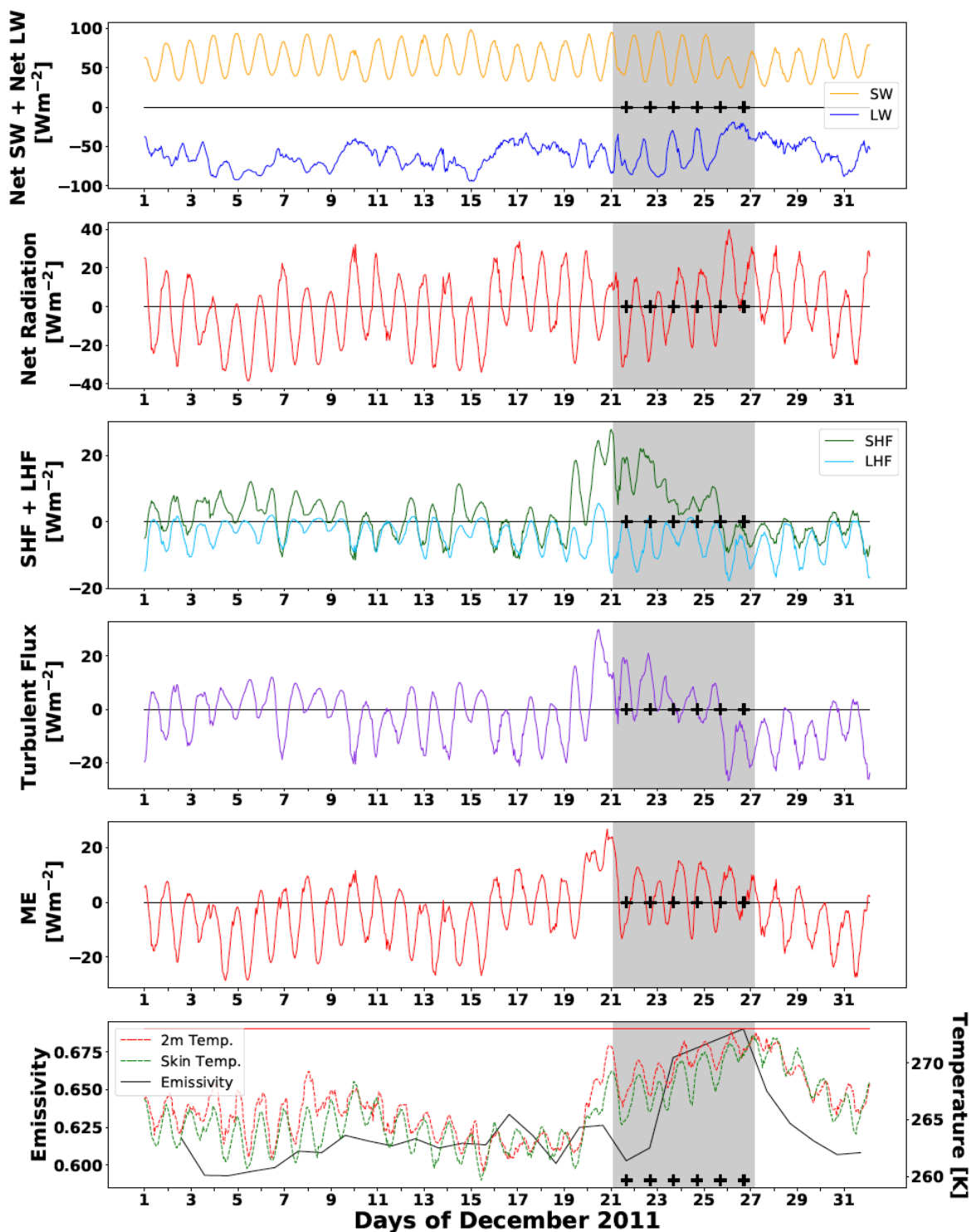
Figure 9. As in Figure 6, but over the Siple Dome region throughout December 2011.
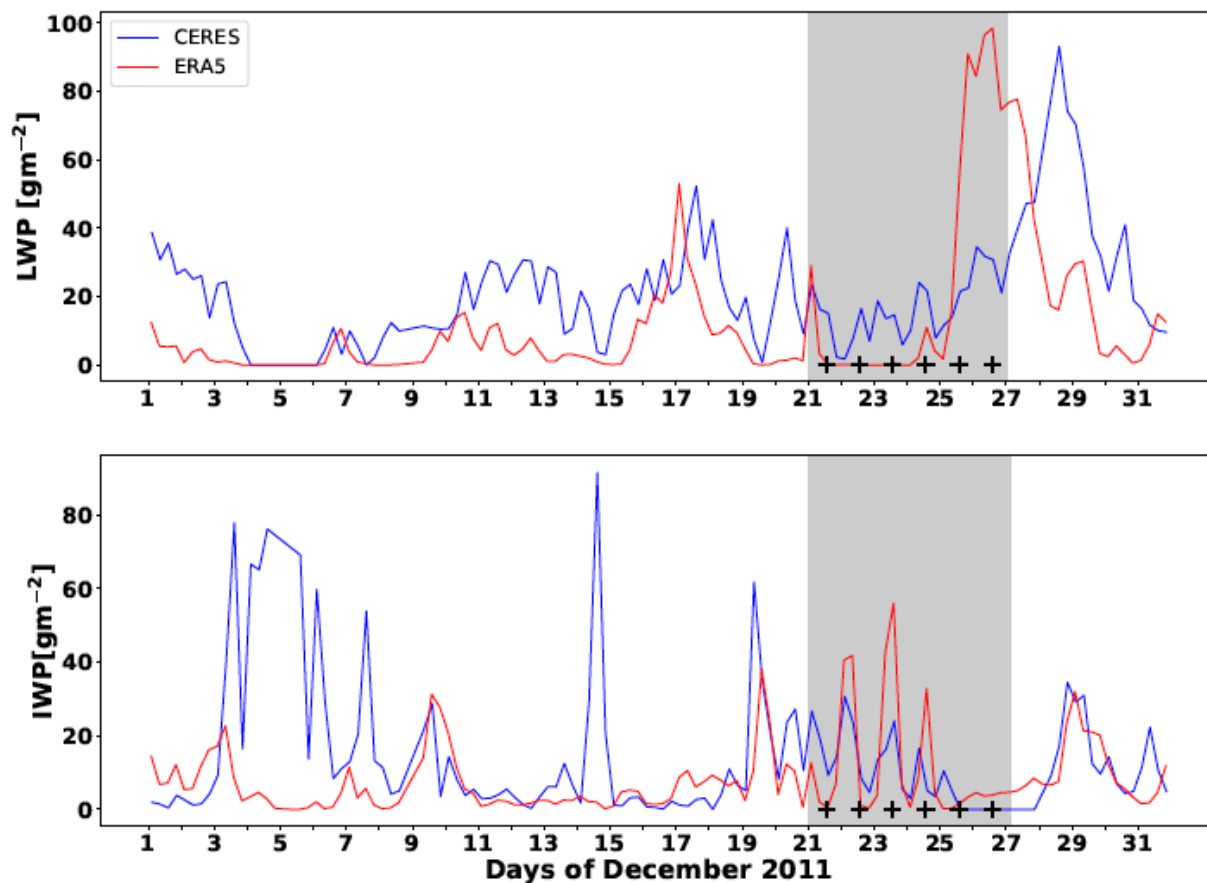
Figure 10. As in Figure 7, but over the Siple Dome region throughout December 2011.

340

Field camp observations indicate cloud cover ranging from scattered to overcast between 22-25 December, with most observations also showing reduced visibility in freezing fog, drifting snow or blowing snow. On 24 December an overcast layer is noted at 2350 UTC with cloud base 1400 m and light snowfall. Throughout 26 December the ceiling is obscured by mist, freezing fog or drifting snow. On 27 December a low overcast is recorded throughout most of the day with cloud base

345 ~300 m. These observations are qualitatively consistent with the radiative flux components of Figure 9a,b and the cloud properties of Figure 10.

3.3 Pine Island and Thwaites Glaciers December 2011

350 Over the Pine Island and Thwaites Glaciers region, satellite PMW T_b shows signatures of melt detected during 19-22 December (Figure 11a), the same time that a SH flux impulse affected Siple Dome with satellite PMW melt detection two days later. These satellite melt signatures over Pine Island and Thwaites Glaciers lasted until 25 December. Examining the surface emissivity samples (Figure 11b) we see much more spatial variability throughout the month than over Siple Dome. Between 2-18 December some of the grid cells show surface emissivity in the "dry snow" range (<0.75), while others are in a range

355 (>0.80) that may signify wet or otherwise altered firn. We notice in Figure 11a that the top of the T_b range in all days between 1-18 December is near or slightly above the standard 30 K melt detection threshold. In Figure 9b the sampled percentiles are referenced to the maximum T_b on 21 December. We notice that the sampled grid cells reaching the 75th and 99th percentiles had very low surface emissivity earlier in the month. Figure 11b therefore illustrates complexity in local-scale surface properties at these low elevation locations near the coast. In contrast, we did not find substantial spatial variability in the ME

360 components when sampled as in Figure 11b, and radiative properties are much more spatially homogeneous over all three regions considered here.

At this location the melt period of interest is between 19-25 December (Figure 12), starting and ending two days earlier than at Siple Dome under the same synoptic conditions. The radiative fluxes (Figure 12a,b) are consistent with optically thick clouds

365 attenuating the SW flux and driving the new LW flux to nearly zero, particularly on 20-21 December and 23-24 December. SH flux (Figure 12c) is small but positive over two diurnal cycles 19-20 December, but this is partially offset by negative LH fluxes, such that the net turbulent flux (Figure 12c) drops below zero every day between 19-25 December (and throughout the month). The total $ME > 0$ across the diurnal cycles 20-22 December and 23-24 December, mainly due to the impact of cloud cover on the radiative fluxes (Figure 12e). The result is steadily rising 2m air and skin temperatures (Figure 12f), with

370 corresponding rise in the fraction of grid cells showing satellite melt detection signatures (Figure 11a).

The cloud properties (Figure 13) show impulses of high LWP and IWP simultaneously detected in CERES remote sensing data and simulated by ERA5. The LWP simulated by ERA5 is twice as large as that retrieved by CERES, and the radiative transfer model providing the fluxes in Figures 12a,b responds to this high LWP. The IWP is consistent between ERA5 and CERES,

375 but we note that both could be artifacts: the ERA5 values might be an overestimate per Silber et al. (2019), and the CERES retrievals could also be an overestimate based on occasional difficulties in phase discrimination when using MODIS spectral reflectances. Nevertheless, the information within the melt period of interest in Figure 13, specifically the total cloud water path (liquid plus ice), is highly consistent with optically thick clouds that provide most of the thermal blanketing effect in this case study.
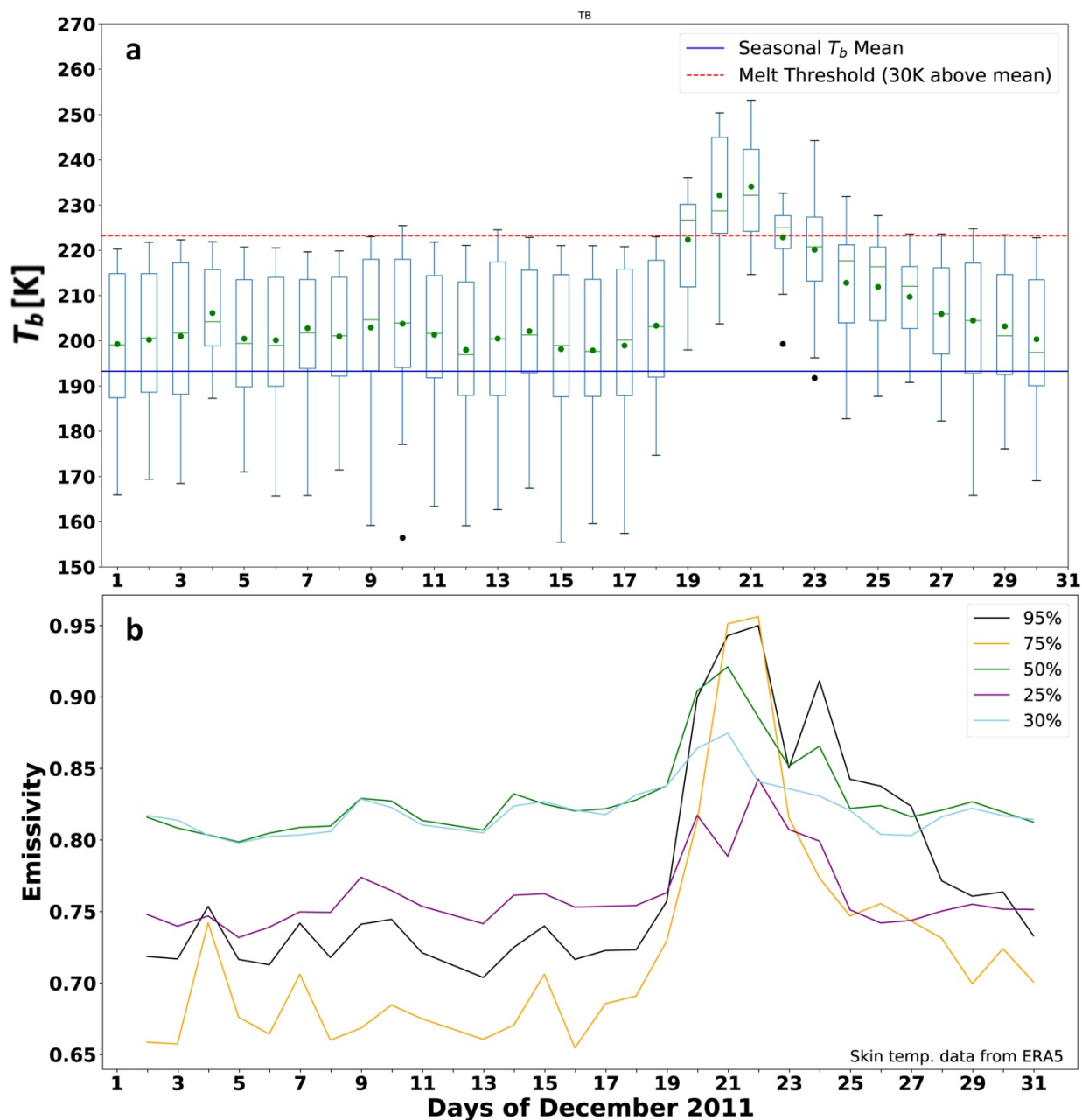
Figure 11. As in Figure 5, but over the Pine Island and Thwaites Glaciers region throughout December 2011. The five estimates of surface emissivity in (b) sampled from the region are referenced to the maximum T_b value in the region on 21 December.
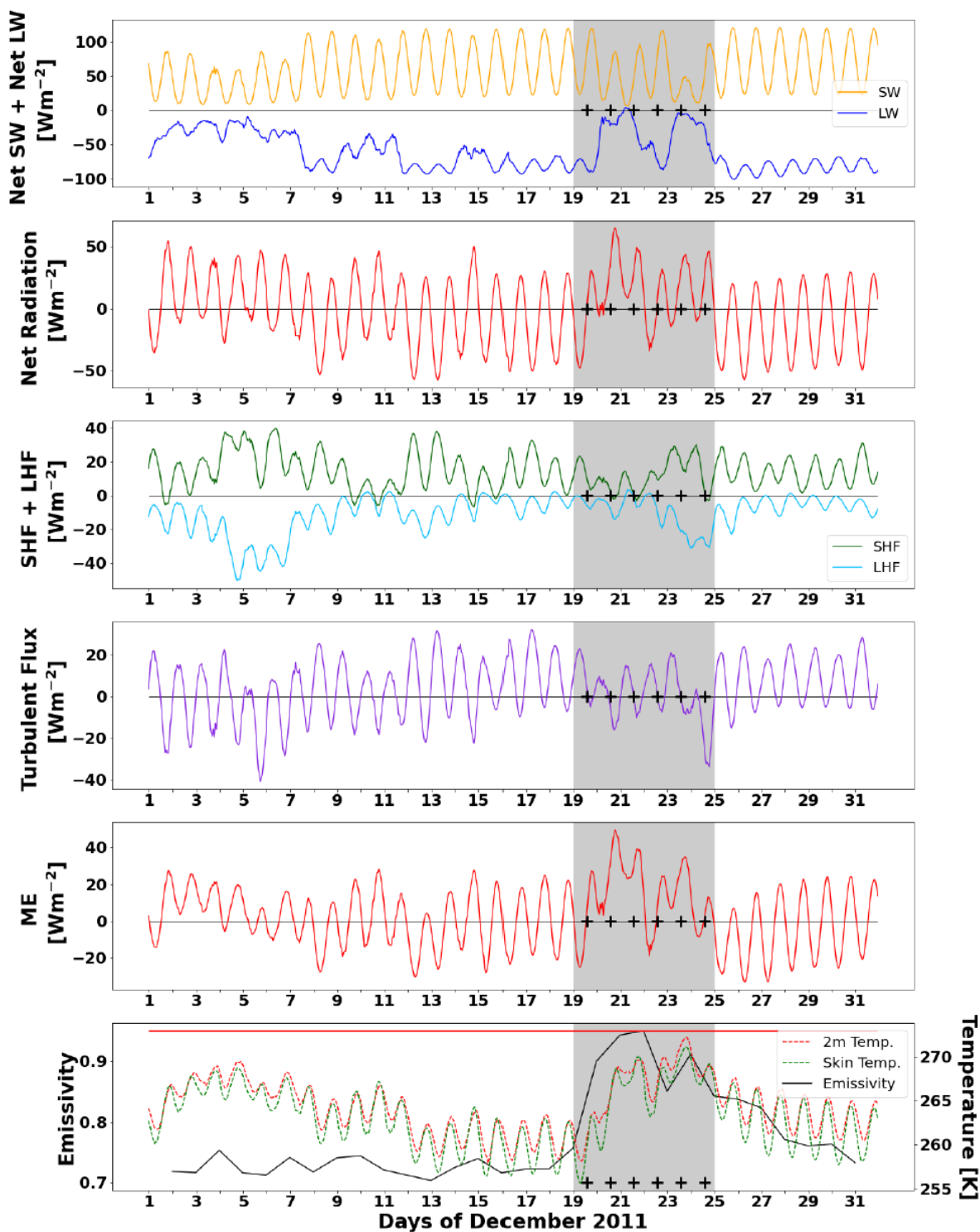
385

Figure 12. As in Figure 6, but over the Pine Island and Thwaites Glaciers region throughout December 2011.
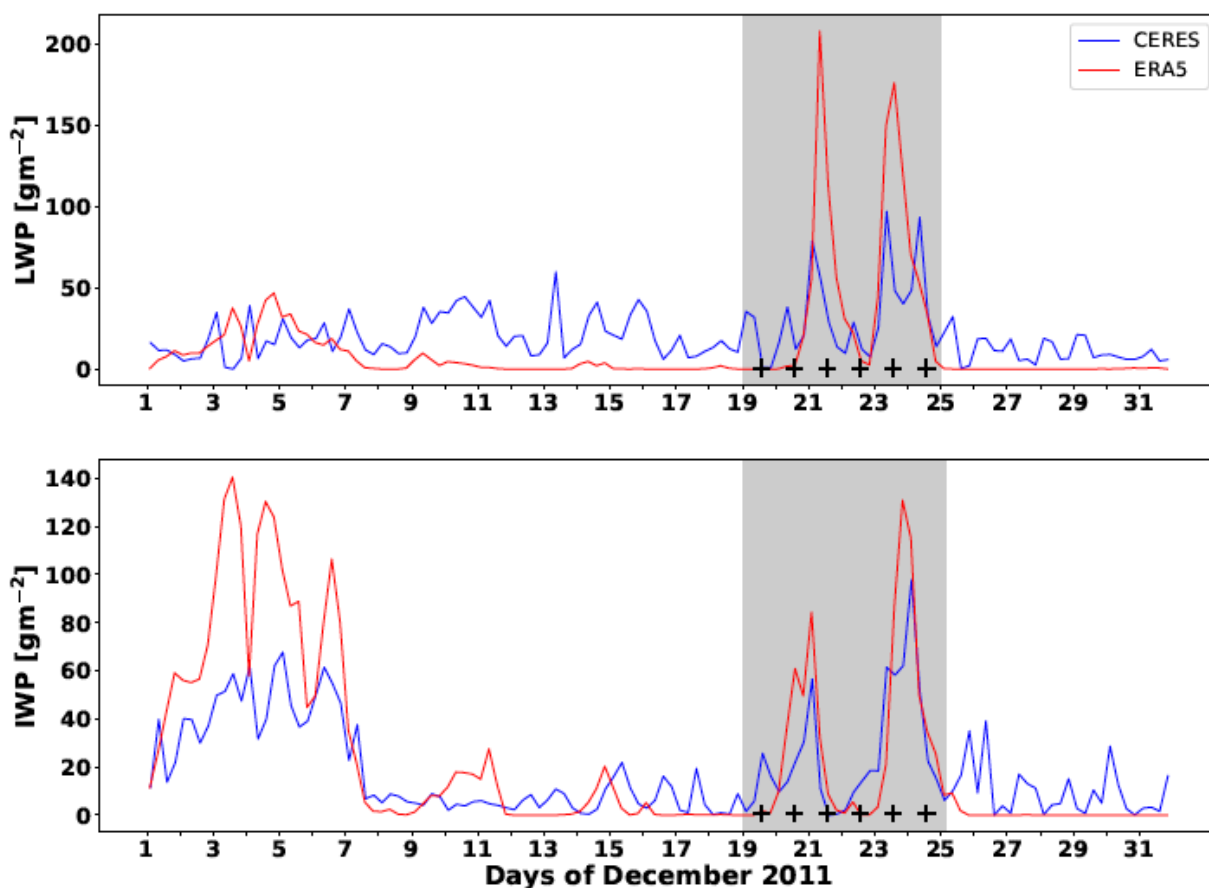
Figure 13. As in Figure 7, but over the Pine Island and Thwaites Glaciers region throughout December 2011.

390

A field camp on Pine Island Glacier recorded mostly few and scattered clouds between 20-27 December. The timing of the two periods of increased sky coverage is consistent with the maxima in *LWP* and *IWP* of Figure 13. Late on 20 December and early on 21 December, the sky became broken to overcast with cloud base 1800 m. During 24 December the visibility dropped to 100-800 m in freezing fog and blowing snow. These observations do not definitively indicate optically thick clouds, and it

395 is possible that this specific field camp location had lighter cloud cover than average for the entire region considered in this case study.

3.4 Pine Island and Thwaites Glaciers January 2012

We next consider these critical ice sheets during January 2012, which saw strong positive southern annular mode (SAM) conditions in conjunction with a weak pressure ridge building off of the southern tip of South America. This briefly diverted

400 the circumpolar westerly flow toward the ASE region. This is an example of melt occurring during a synoptic condition for which melt is not very frequent (Scott et al., 2019). Our period of interest shows a modest melt signal (Figure 14a), with the mean satellite PMW T_b reaching the standard 30 K detection threshold only on 6 January. However, we note that throughout January 2012 the upper bound of the T_b sample is near or slightly above the 30 K detection threshold. In Figure 14b we see that all the sampled surface emissivity estimates are larger than 0.8, in contrast to the lower values observed over Siple Dome

405 outside of melt periods.

During our period of interest 4-8 January, the radiative fluxes show a strong modulation by cloud cover (Figure 15a), with net SW flux attenuated by nearly a factor of two relative to most of the rest of the month, and with net LW driven to nearly zero. The result is that the net total radiative flux remains positive across three diurnal cycles. The SH and LH fluxes (Figure 15c)

410 are much smaller in amplitude and the net turbulent flux drops below zero every day (Figure 15d). It is primarily the radiative flux terms that keep the *ME* positive across nearly four diurnal cycles (Figure 15e). The corresponding 2m air and skin temperatures rise steadily during this interval to a monthly maximum on 7 January (Figure 15f) which is the second strongest day in the satellite melt detection signal (Figure 14a). We note that two other short periods, 16-17 January and 20-21 January, show *ME* > 0 across two diurnal cycles. However, the 2m air and skin temperatures are well below freezing during these

415 periods, and satellite melt signatures are barely detectable (Figure 14). During 4-8 January the 2m air and skin temperatures approach freezing, which is generally necessary for melt onset even when the primary energy input is from a cloud radiative impulse.

The cloud *LWP* estimates (Figure 16a) show consistency between ERA5 and CERES during 4-8 January, although ERA5

420 appears to underpredict *LWP* for most of the rest of the month. ERA5 again appears to overpredict *IWP* during the melt period of interest, by more than a factor of two compared with CERES. During 4-8 January the CERES *LWP* is mostly within the thin cloud range (10-40 g m^{-2}) associated with the Bennartz et al. (2013) all-wave radiative effect. CERES *IWP* is almost as large as the *LWP*, which again may reflect errors in MODIS-based phase discrimination. Considering the CERES combined *LWP* and *IWP*, it remains unclear if the cloud radiative impulse (Figure 15a,b) is due to the Bennartz et al. (2013) all-wave

425 effect or to thermal blanketing by optically thicker cloud cover. And the ERA5 radiative transfer algorithm produces the fluxes in Figure 15a using the large cloud *IWP* values that are almost certainly in error. This case study clearly shows the role of clouds in altering the *ME* to enhance surface melt, but also underscores the need to improve both satellite retrieval and reanalysis cloud microphysics to obtain a complete understanding.

430 The field camp on Pine Island Glacier recorded broken to overcast cloud cover with bases 300-600 m on 4 January, with ceilings dropping to 150 m on 5 January. On 6-7 January at least two cloud layers were observed, with variable ceilings mostly below 2000 m. Throughout 8 January sky coverage steadily reduces from broken to scattered/few. Light snowfall is the most
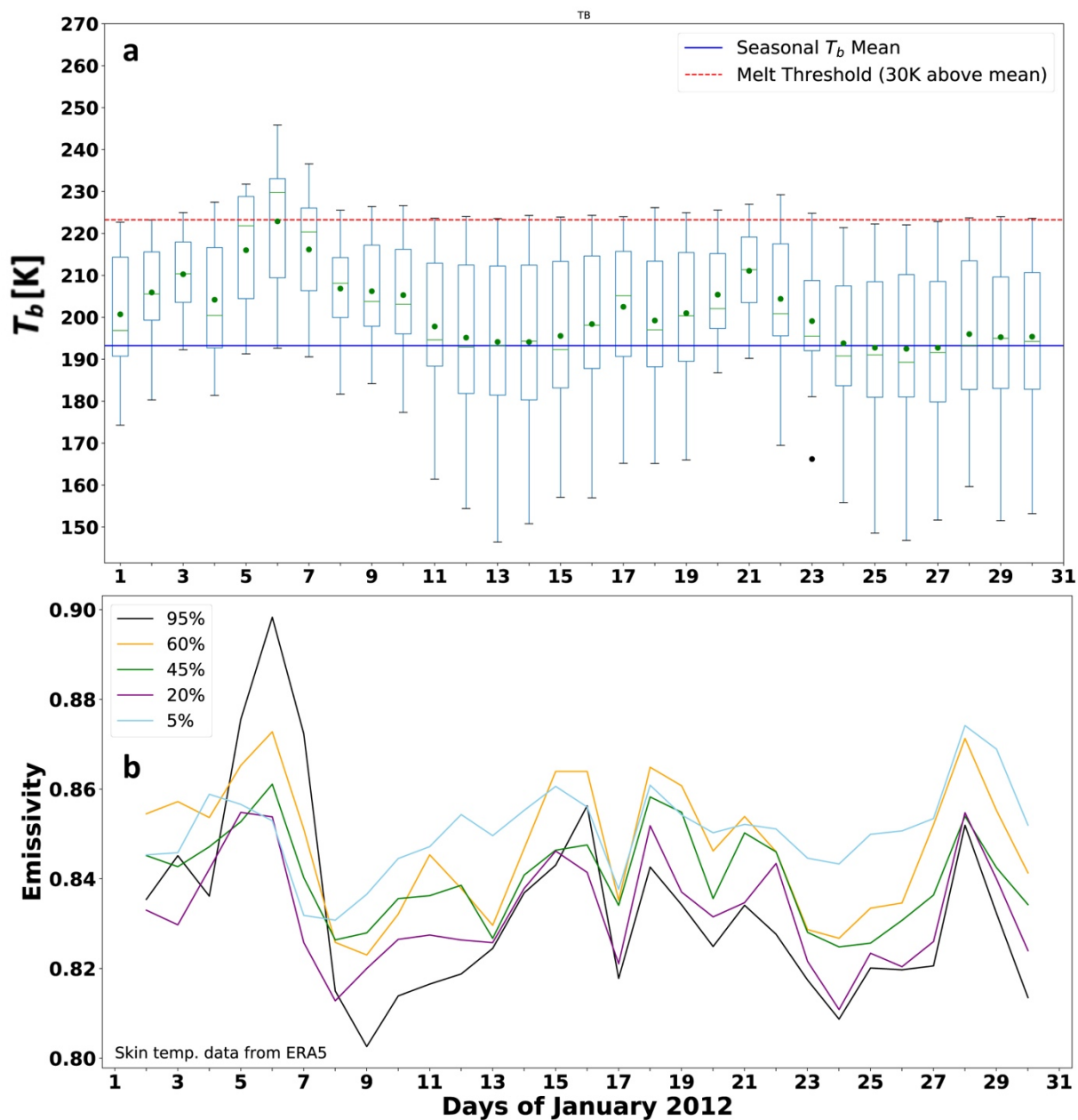
Figure 14. As in Figure 5, but over the Pine Island and Thwaites Glaciers region throughout January 2012. The five

435   estimates of surface emissivity in (b) sampled from the region are referenced to the maximum T_b value in the region on
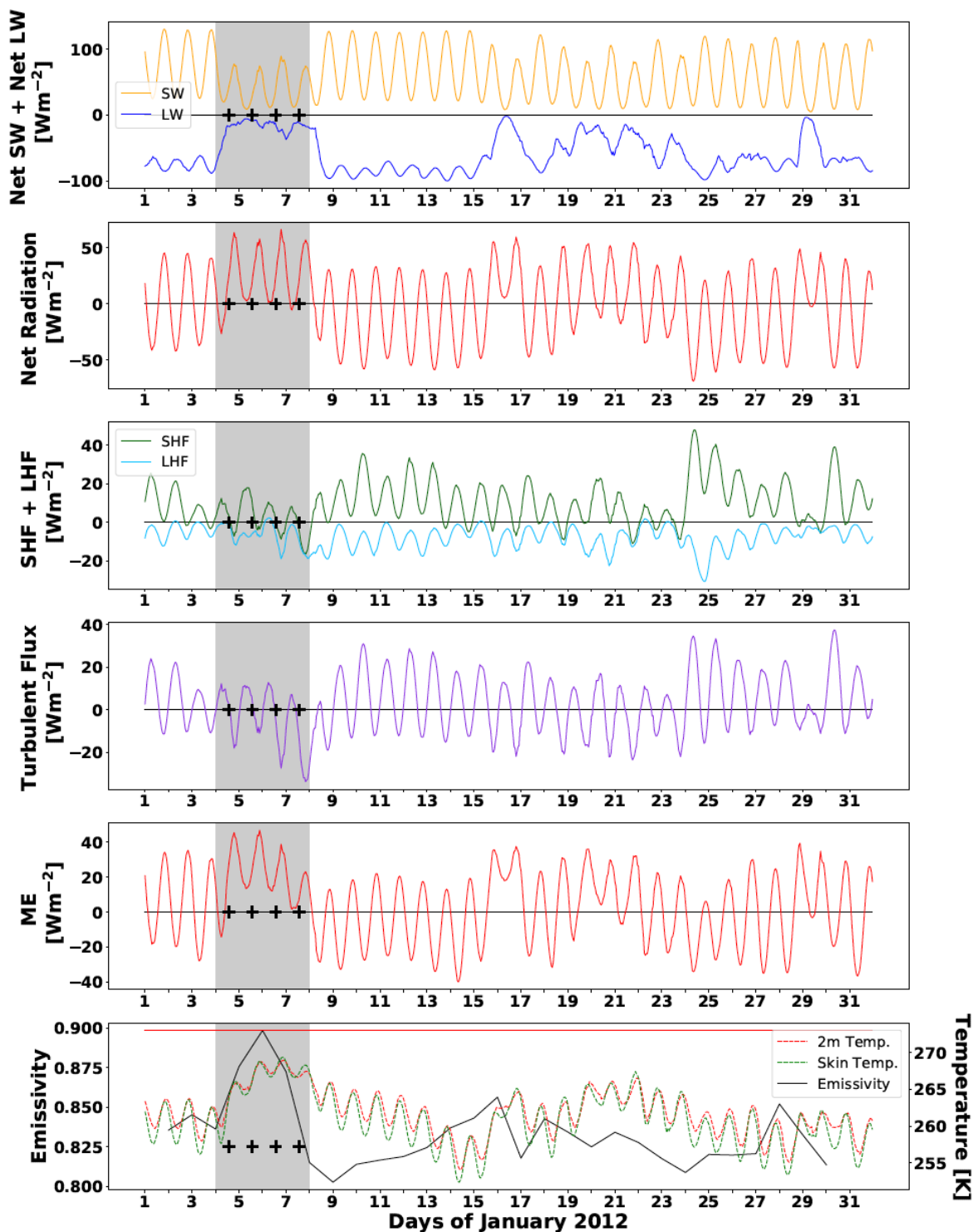
6 January.

Figure 15. As in Figure 6, but over the Pine Island and Thwaites Glaciers region throughout January 2012.
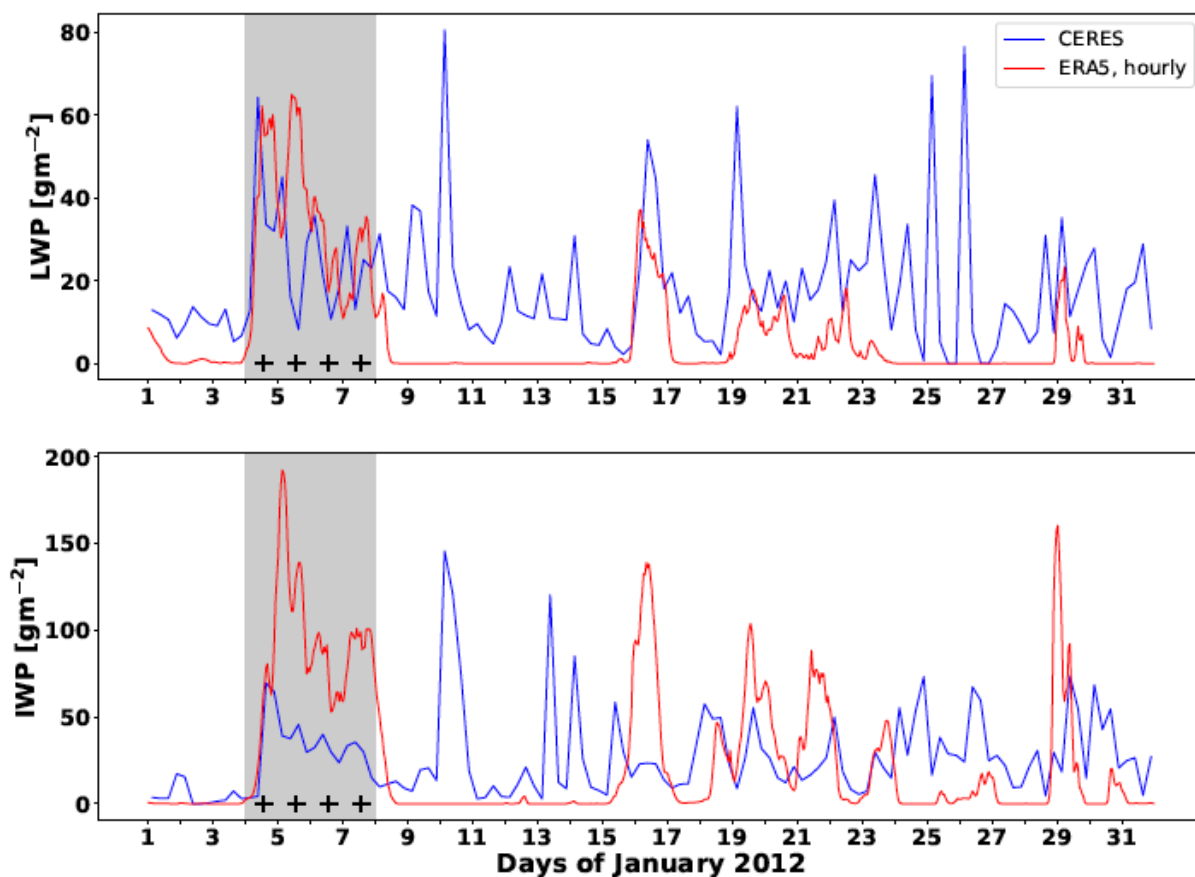
Figure 16. As in Figure 7, but over the Pine Island and Thwaites Glaciers region throughout January 2012.

consistent present-weather condition between 4-8 January, but there are also episodes of mist, freezing fog, drifting snow and blowing snow. Qualitatively these observations might suggest optically thicker cloud cover.

3.5 Pine Island and Thwaites Glaciers February 2013

We now examine a surface melt event that appeared in late summer 2013, when climatological surface and lower tropospheric temperatures are several degrees lower than in January. In February 2013, a strong pressure ridge built up and remained stationary over the Amundsen-Bellingshausen Sea region. The combination of this and a low-pressure system over the Ross Sea set up warming conditions for the Amundsen Sea Embayment, where an anomalously strong zonal pressure gradient facilitated meridional flow toward the area. This synoptic pattern is representative of frequent surface melting in the area (Scott et al., 2019). In Figure 17a, satellite PMW data show a three-day, partial-surface-melt signature in the Thwaites and Pine Island Glaciers region from 20-22 February 2013. As for the December 2011 case study, surface emissivity (Figure 17b) has relatively large spatial variability throughout this local region.
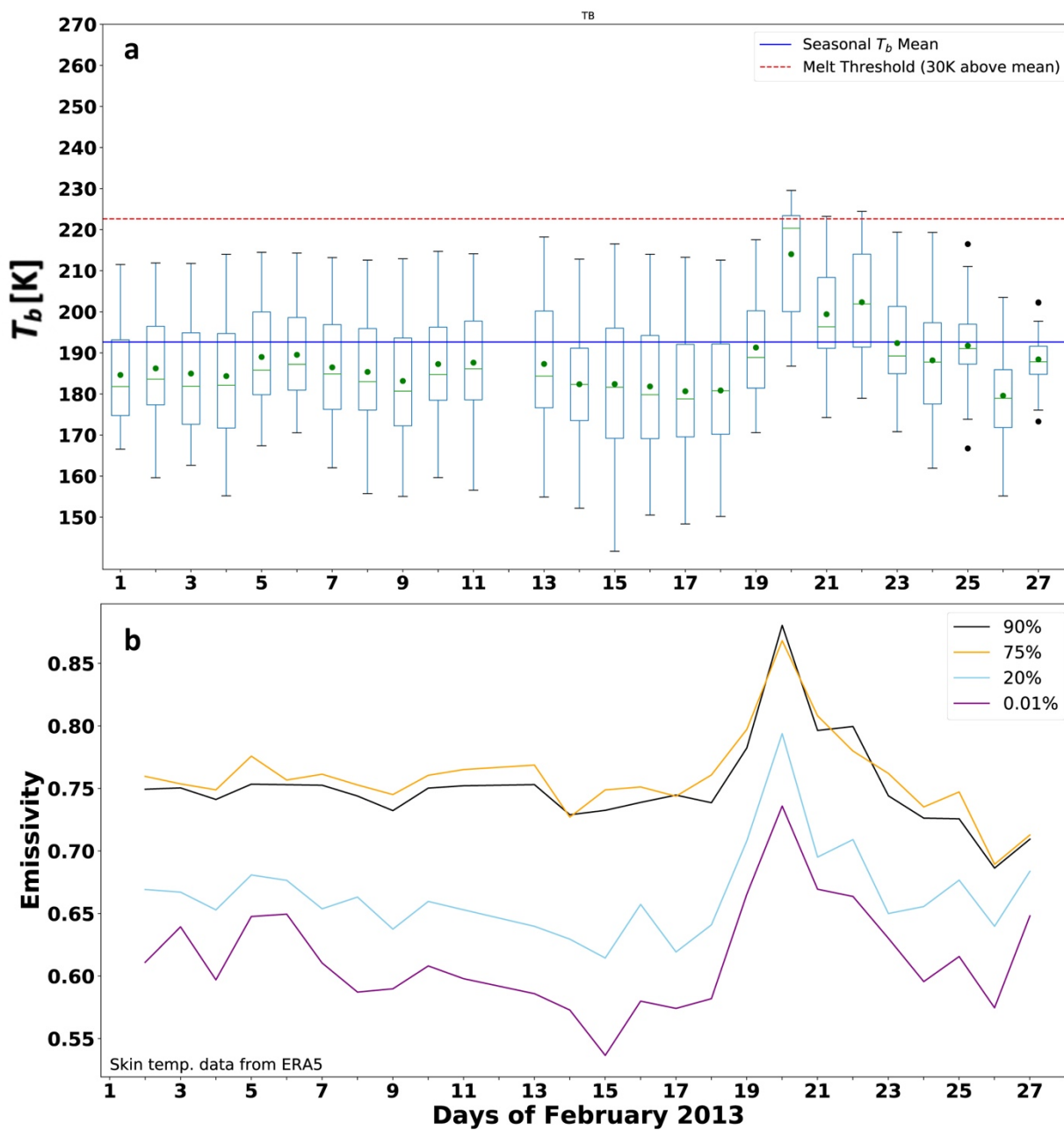
Figure 17. As in Figure 5, but over the Pine Island and Thwaites Glaciers region throughout February 2013. The five

455   **estimates of surface emissivity sampled in (b) from the region are referenced to the maximum T_b value in the region on**

    20 February.

For our melt period of interest between 19-21 February, the radiative fluxes (Figure 18a) show a clear signature of thermal blanketing by optically thick cloud cover. The new SW flux is attenuated by a factor of three compared with the earlier weeks

460   in February, such that its diurnal amplitude is only ~20 W m^{-2}. The LW flux is positive, signifying optically thick clouds that are warmer than the surface. The net radiative flux (Figure 18b) is positive over the diurnal cycles 20-21 February. We also find positive SH flux (Figure 18c) that yields positive net turbulent flux (Figure 18d) across the entire melt period of interest. This positive turbulent flux is comparable in magnitude if not greater than the net radiative flux between 19-21 February. Then between 21-23 February, as the cloud radiative effect diminishes such that the net radiation drops below zero each day, the SH

465   flux doubles in magnitude to sustain the positive ME until 23 February (Figure 18e). The result is a steady rise in 2m air and skin temperatures from 20 February, when the satellite melt signature is first detected, to nearly freezing by 21 February and staying this warm for another four days. Even though these temperatures remain close to freezing for several days, the satellite melt signature decreases as the ME decreases and resumes a diurnal cycle that drops below zero.

470   The cloud properties during this melt period (Figure 19) are mainly consistent with large optical thickness. The CERES average LWP and IWP are 34.9±25.8 g m^{-2} and 47.8±27.4 g m^{-2}, respectively. While this larger IWP may reflect errors in phase discrimination, the suggested total cloud water content is higher than that associated the Bennartz et al. (2013) all-wave effect, and instead indicates primarily a longwave surface warming where a low cloud radiates as a blackbody, with a muted SW diurnal signal. ERA5 LWP and IWP are significantly larger than the CERES retrievals, and may be overestimates due to

475   microphysical errors, but their timing is consistent with the CERES detection of optically thick clouds. In this case study, we therefore see a thermal blanketing effect that is initiated in the first two days by a cloud radiative warming, and then sustained for another two days by elevated SH flux.

3.6 Ross Ice Shelf December 2011

Our final case study returns to the December 2011 synoptic conditions, in a location on the RIS adjacent to the Transantarctic

480   mountains (Figure 1) where föhn winds play a role in localized surface melt (Figure 1). Figure 20a indicates that between 23-25 December, some grid cells show a strong satellite PMW melt signature, and a few continue to show a melt signature as late as 27 December. Similar to Siple Dome, surface emissivity is spatially uniform and consistent with a dry snow surface throughout the previous three weeks of December (Figure 20b). Figure 21 shows ERA wind speed and direction at the surface and at 850 hPa. Between 9-19 December winds are light to moderate, and have a variety of directions but are mostly northerly

485   between 9-14 December and 18-19 December. During the melt period 23-25 December, surface and lower troposphere winds strengthen and their directions become more spatially uniform, mainly easterly to southeasterly, consistent with descent into the region from the Transantarctic mountains.
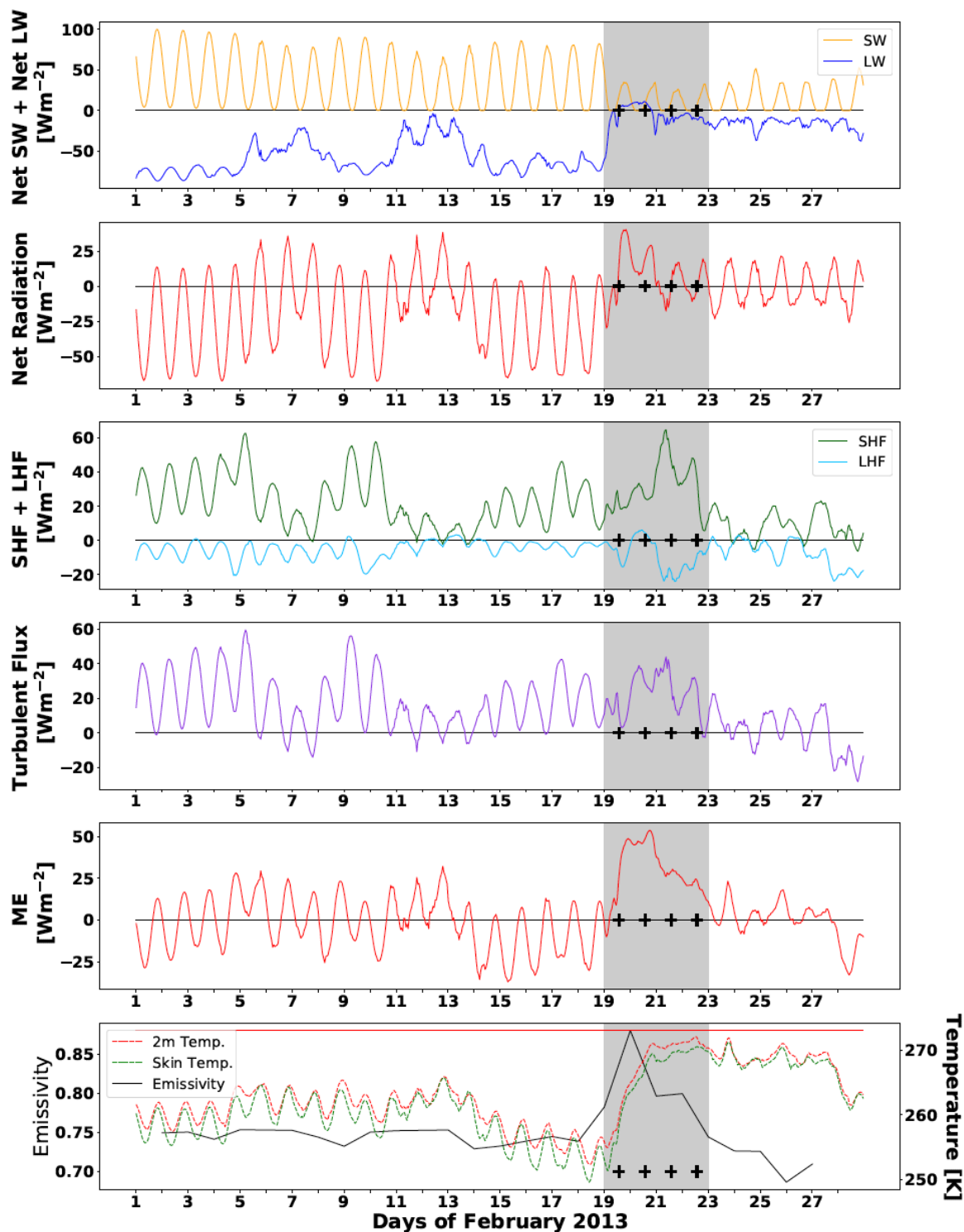
Figure 18. As in Figure 6, but over the Pine Island and Thwaites Glaciers region throughout February 2013.
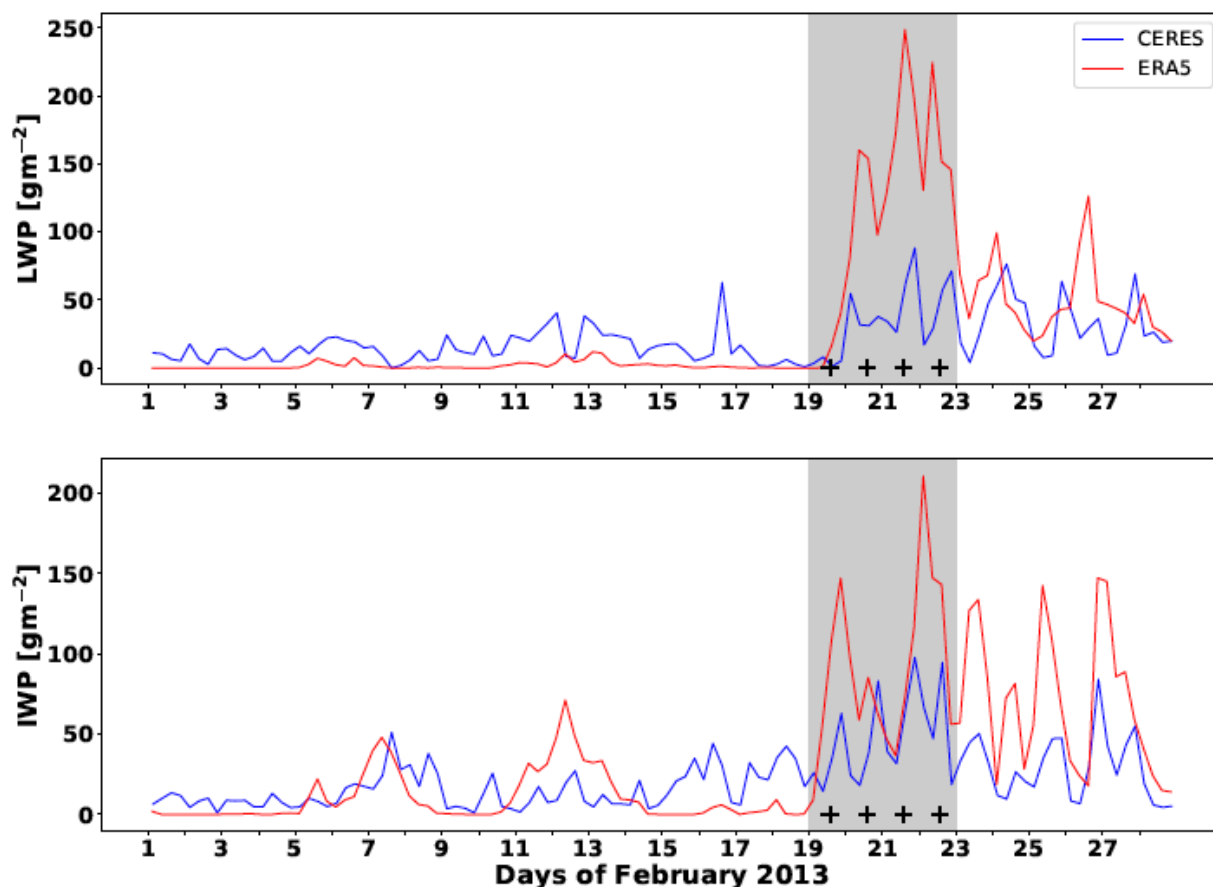
Figure 19. As in Figure 7, but over the Pine Island and Thwaites Glaciers region throughout February 2013.

Similar to the Siple Dome case for December 2011, the relevant energy inputs appear to precede the satellite melt signature

495   detection by approximately two days. For the SEB components (figure 22) we have identified the study period of interest as 19-23 December, while the satellite melt signature occurs mainly on 23 December and later. The radiative fluxes during 20-22 December (Figure 22a) show net SW attenuation and LW increase toward zero that appear consistent with all-wave enhancement from optically thin cloud. During this interval the net radiative flux is mostly positive, but does briefly drop to zero each diurnal cycle (Figure 22b). A strong impulse of positive SH flux (Figure 22c) is partly canceled by a LH flux of

500   opposite sign, but the net turbulent flux is positive across two diurnal cycles 20-21 December (Figure 20d), as is the total *ME* (Figure 22e). The maximum in *ME* on 21 December corresponds with a local maximum in 2m air and skin temperatures (Figure 22f), which increased nearly 10K until they are close to freezing. The ERA5 daily maximum in 2-m air temperature continues to rise to above freezing on the 24th and peaking on the 25th, before returning to sub-zero temperatures. Cloud properties between 19-23 December (Figure 23) show ERA5 simulated and CERES detection of cloud cover that are consistent
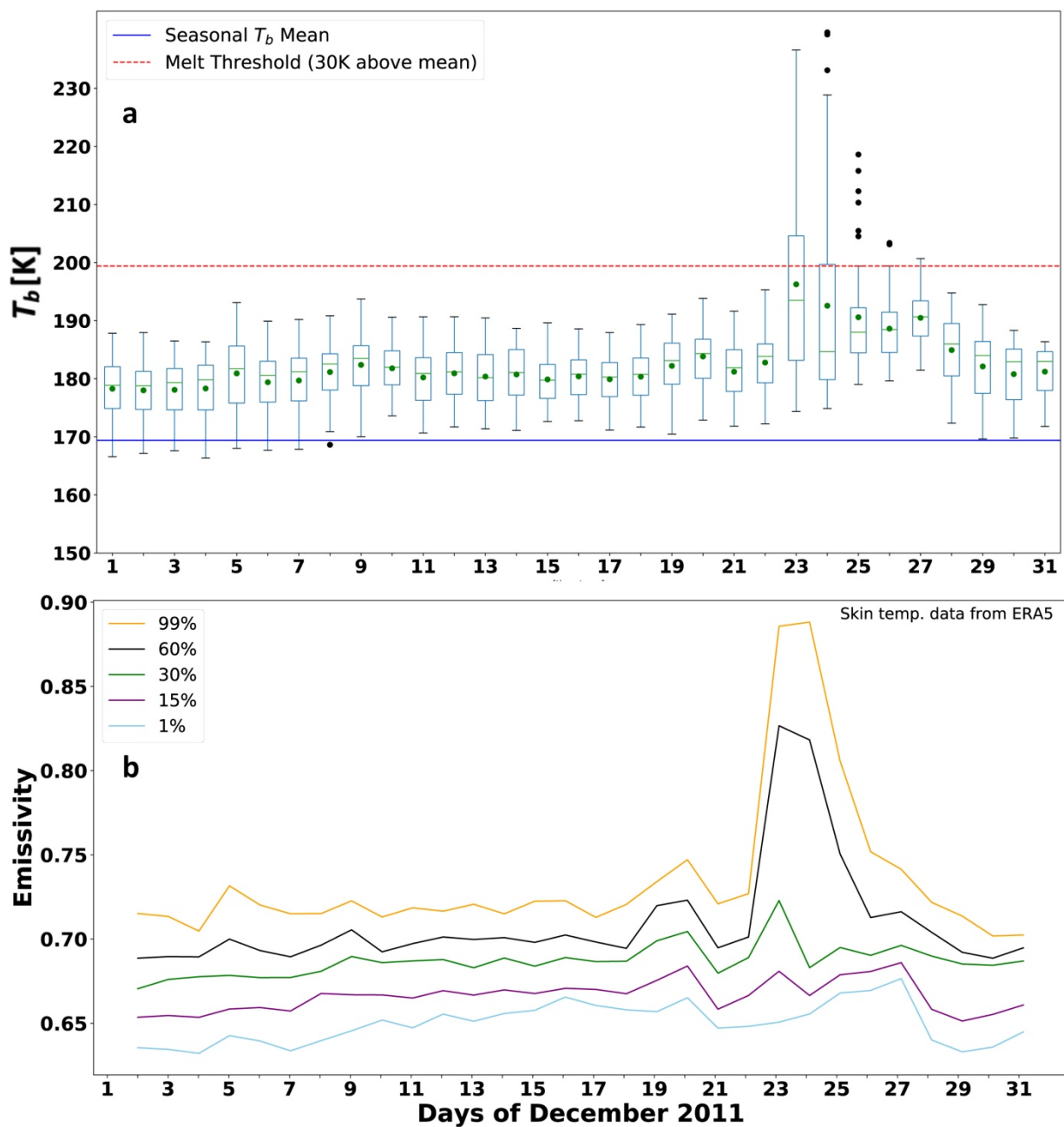
505

Figure 20. As in Figure 5, but over the RIS region containing the Tom and Sabrina AWS, throughout December 2011. The five estimates of surface emissivity sampled in (b) from the region are referenced to the maximum T_b value in the region on 23 December.
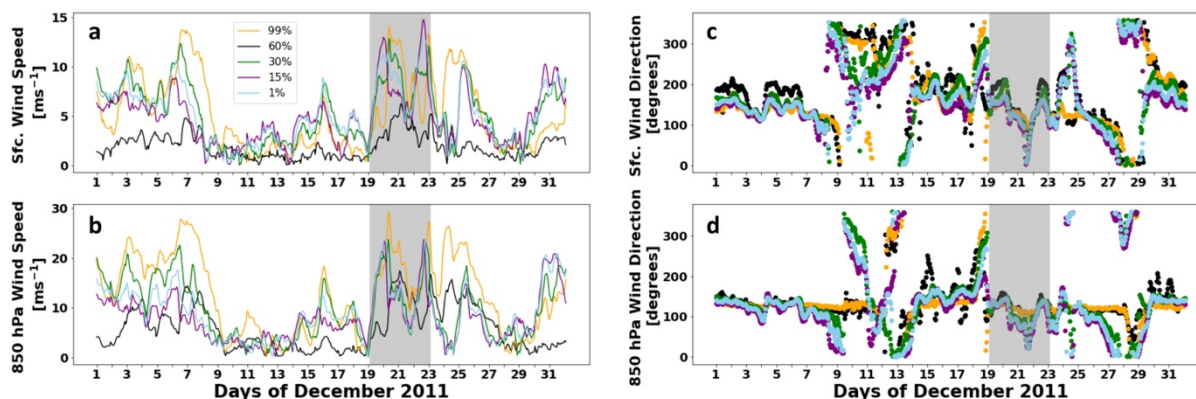
510 **Figure 21. Time series of sampled ERA5 (a) near-surface wind speed, (b) 850 hPa wind speed, (c) near surface wind direction, (d) 850 hPa wind direction over the RIS region containing the Tom and Sabrina AWS, throughout December 2011. Percentiles sampled correspond to the locations of Figure 18b.**

in time, and subject to the same potential uncertainties and errors as in the previous case studies. With CERES *LWP* and *IWP*

515 values of 14.7 ± 11.0 g m^{-2} and 32.7 ± 16.1 g m^{-2}, respectively, the clouds are likely to be optically thin and causing an all-wave radiative enhancement.

In Figure 24 we examine in situ measurements of 2m air temperature, wind speed and wind direction from the Tom and Sabrina AWS. During the time intervals 9-19 December and 19-23 December, these measurements are very consistent with the ERA5

520 values (Figure 21). However, between 23-26 December surface wind speed is consistently stronger and wind direction is more consistently southeasterly at both AWS than in the ERA5 reanalysis data, although the 2m surface air temperatures compare well. A possible cause of this discrepancy might be the coarse spatial resolution in ERA5, yielding an underprediction of föhn winds (e.g., Trusel et al., 2013). The ERA5-based analysis (Figures 21-22) suggests that the initial fohn wind onset combined with a cloud radiative enhancement gradually set up the conditions starting on 20 December that lead to satellite PMW melt

525 signature detection on 23 December. Absent the cloud radiative enhancement after 22 December, the AWS data suggest that persistent fohn winds alone can sustain the surface melt conditions for several more days. We do note that the underprediction of fohn winds in ERA5 might be offset by larger LWC and IWC that are retrieved in the CERES data (Figure 21).

Finally, we note that between 1-9 December there are strong surface and lower troposphere winds from a southeasterly

530 direction, seen in both ERA5 and AWS, that induce consistently positive SH flux and positive net turbulent flux over at least three diurnal cycles. These observations would also be consistent with fohn winds from the Transantarctic mountains. Skin temperatures and 2 m air temperatures are also 3-5 K warmer than during the subsequent time interval 9-19 December. However, cloud cover appears to be consistently light in both the ERA5 simulations and CERES retrievals (Figure 23) that
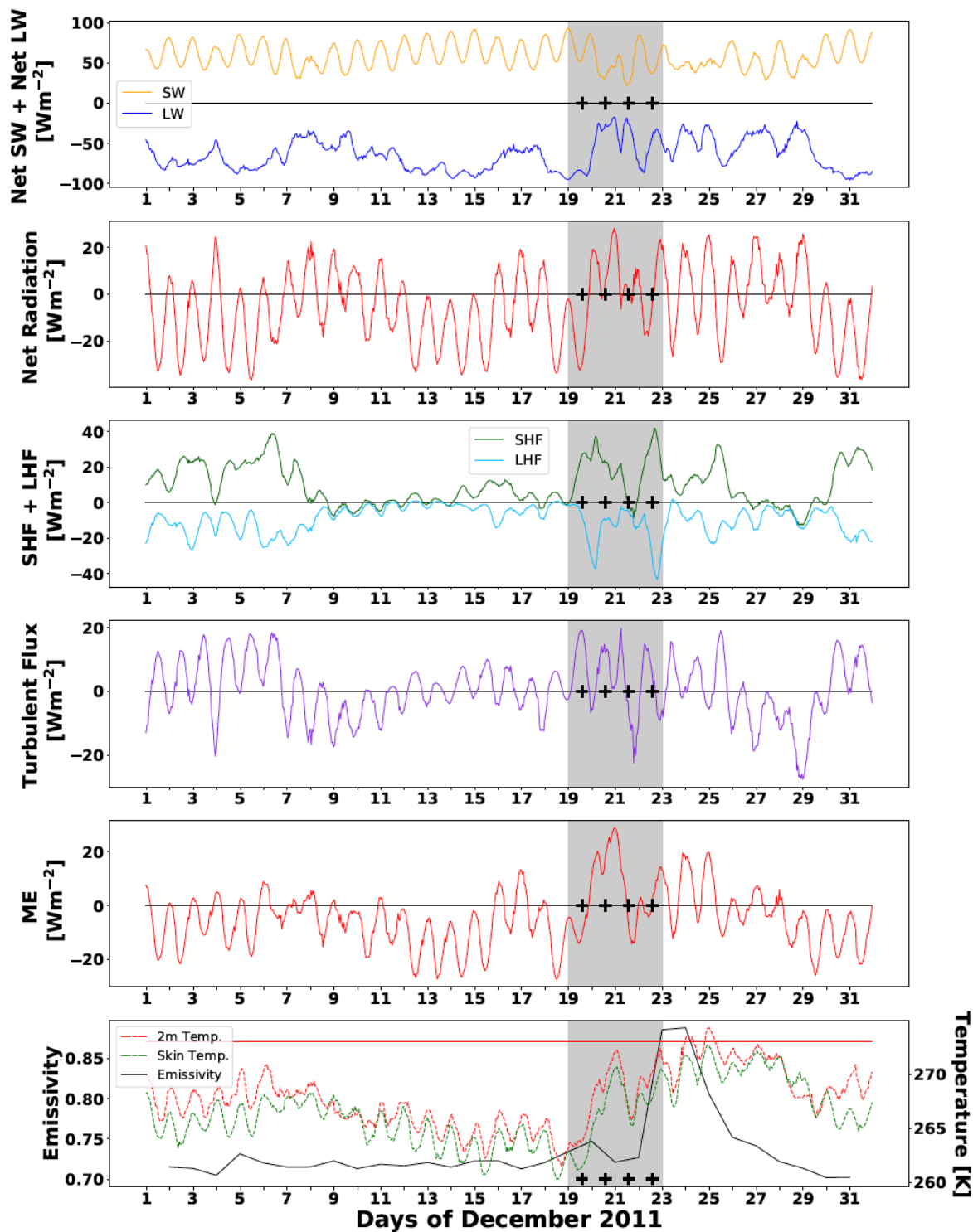
535   **Figure 22. As in Figure 6, but over the RIS region containing the Tom and Sabrina AWS, throughout December 2011.**
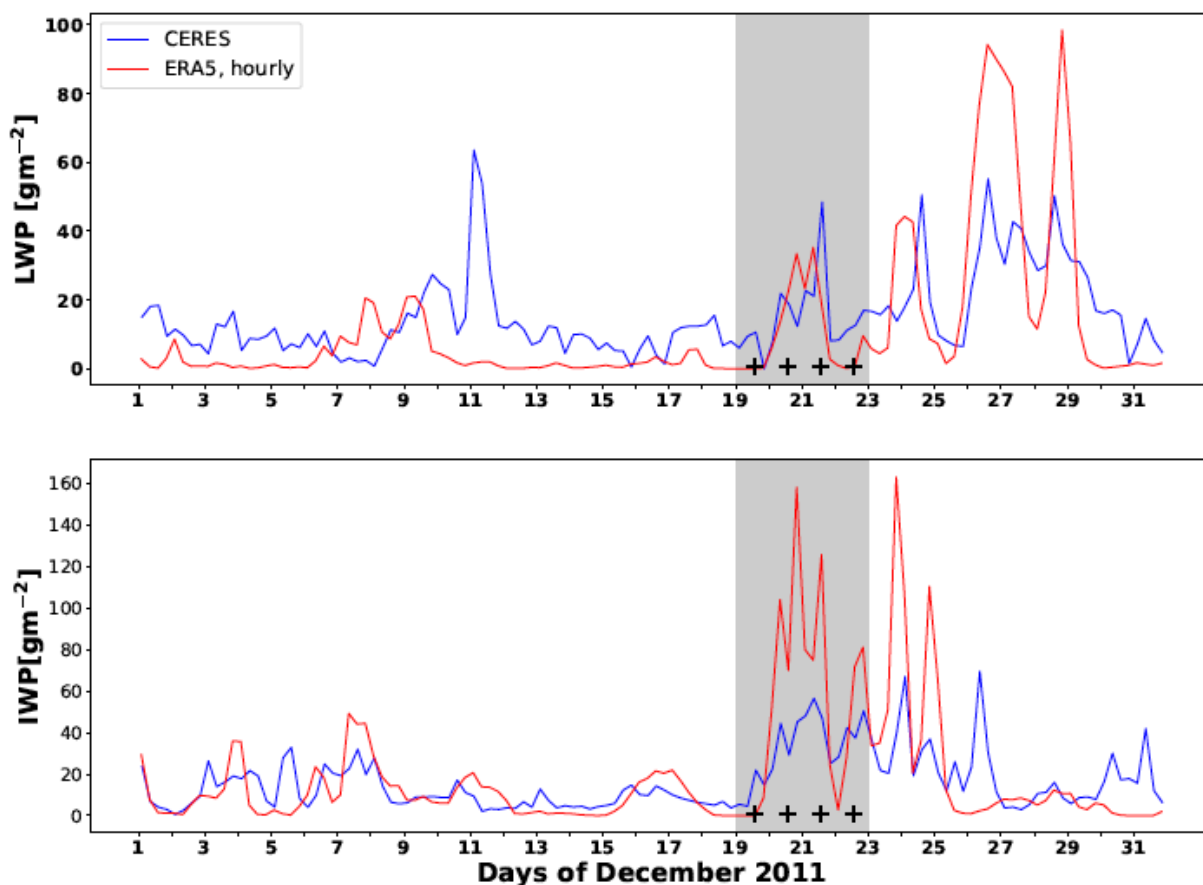
Figure 23. As in Figure 7, but over the RIS region containing the Tom and Sabrina AWS, throughout December 2011.

540   allows for LW cooling (Figure 22a), and the total ME remains mostly negative before 19 December. Early in December the synoptic conditions discussed above have not yet set up the warm air intrusion that brings moisture and cloud cover to all three locations. A downslope wind by itself may not be sufficient to cause a detectable surface melt event (e.g., King et al., 2017), but may need to operate in conjunction with additional conducive atmospheric conditions.

Conclusion

545   In this study we demonstrate that readily available climatic data, including meteorological reanalysis and satellite remote sensing, can be used to examine and diagnose individual episodes of surface melt over Antarctic ice sheet and ice shelf locations that are of significant concern in a steadily warming climate. We demonstrate examples for each of three thermodynamic mechanisms that induce surface melting. The case study from January 2015 over Siple Dome very likely
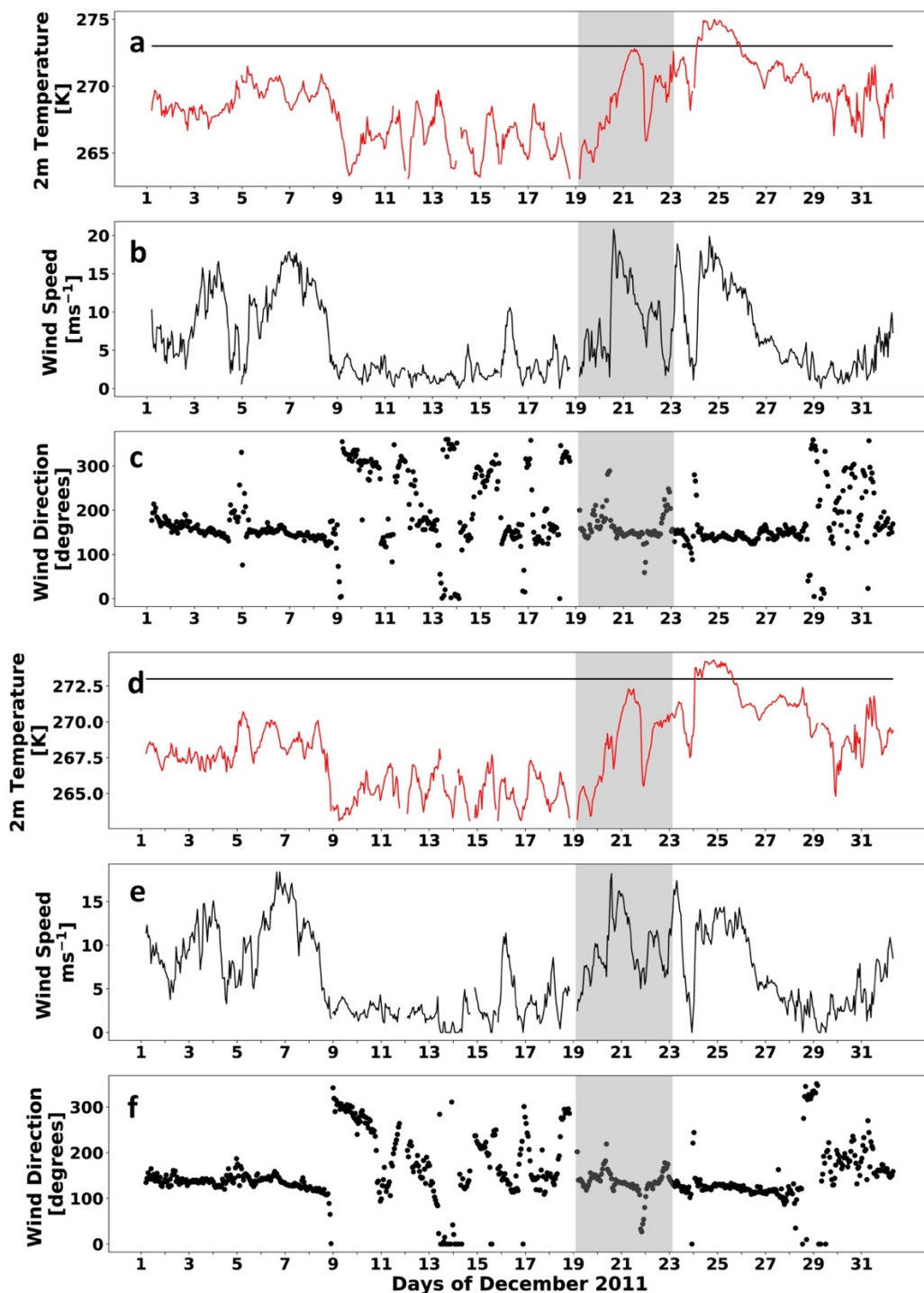
Figure 24. Time series of AWS measurements throughout December 2011: (a) Tom air temperature, (b) Tom wind speed, (c) Tom wind direction, (d) Sabrina air temperature, (e) Sabrina wind speed, (f) Sabrina wind direction.

involves the same all-wave cloud radiative enhancement discovered over the GIS (Bennartz et al., 2013; Van Tricht et al., 2016). In contrast, Pine Island and Thwaites Glaciers during December 2011 experience a thermal blanketing effect where the positive *ME* impulse comes mainly from optically thick clouds. Over the Tom and Sabrina AWS locations on the RIS, we

555 identified a föhn wind effect that might be augmented by an all-wave cloud radiative enhancement. Other examples when two of the mechanisms are at work include the December 2011 thermal blanketing case over Siple Dome, where an impulse of positive SH flux set up the surface conditions for melt onset followed by additional energy input from a cloud radiative enhancement, and the February 2013 thermal blanketing case over Pine Island and Thwaites Glaciers, when optically thick cloud cover initiates a melt event that is subsequently prolonged by positive SH flux.

560

For the Pine Island and Thwaites Glaciers region we notice considerable local-scale variability in surface T_b and emissivity, possibly related to microwave signatures dominated by new snow in some grid cells and by older snow or prior melt events in others. Bell et al. (2017) show that local-scale variability on Antarctic ice shelves influences whether surface meltwater filters into the ice as a source or hydrofracturing or runs off in temporary rivers. Local-scale spatial inhomogeneity on the ice shelves

565 probably requires further investigation to make reliable projections regarding multi-year stress.

Two limitations stand out with the present level of analysis. First, improvements are needed in cloud microphysics and related optical properties in both the reanalysis models and in the satellite remote sensing retrievals. Although the presence of cloud in a case study is reliably detected, the microphysical uncertainties sometimes prevent a full diagnosis of the melt event

570 mechanism. For example, in the January 2012 case study over Pine Island and Thwaites Glaciers, a cloud radiative effect is clearly indicated but it is not clear if this is a thin cloud all-wave effect or an optically thick thermal blanketing effect. In atmospheric models, the use of double-moment cloud microphysical parameterizations makes noticeable improvements over Antarctica (e.g., Hines et al., 2019). However, these more rigorous parameterizations are found mainly in global climate models. Numerical weather prediction models, which are used to generate reanalysis data, must run on an operational forecast

575 schedule and may not be able to accommodate the time-consuming rigorous parameterizations.

In the MODIS-based retrievals contained in the CERES SYN1deg data product, we suspect that some of the higher *IWP* values may actually be liquid water clouds. Chylek et al. (2006) suggest that cloud phase discrimination that relies on differential backscatter in MODIS near-infrared channels can be biased toward the ice phase. The MODIS retrieval algorithms for cloud

580 phase discrimination generally use both near- and mid-infrared bands, and further investigation is needed specific to clouds over West Antarctica to identify possible errors. Additionally, the CERES-MODIS approach can retrieve unrealistically high *IWP* values over ice sheets, mainly over the Antarctic interior. An issue with this approach is that over these areas, where the contrast between the surface and cloud albedo is small, a large correction of cloud water path is necessary to match the TOA fluxes since they are insensitive to small changes. Furthermore, since *LWP* has limited observational constraints over
585 Antarctica, the algorithm likely has to resort to increasing the *IWP* dramatically to compensate for any lack of brightness owing to missing liquid (e.g., Lenaerts et al., 2017).

A second limitation involves quantifying the effect of föhn winds. In the RIS example the AWS data indicate more persistent föhn winds than are simulated by ERA5. This is most likely related to the coarse spatial resolution in the reanalysis model.

590 While ERA5 can identify the likely presence of a föhn wind effect based on its generally accurate lower troposphere wind direction relative to varying high terrain, a more quantitative analysis might need to incorporate detailed knowledge of the actual terrain elevation (Dreschel and Mayer, 2008; Elvidge et al., 2015; King et al., 2017).

Over the modern satellite record spanning nearly four decades, the number of melt events over West Antarctic locations most

595 critical for sea level rise is a reasonable number for this type of analysis. It should be possible to make projections regarding future atmospheric stress on the West Antarctic ice shelves by identifying the specific mechanisms, their frequency of occurrence singly or concurrently, and their relationships with large-scale meteorological drivers (Nicolas and Bromwich, 2011; Scott et al., 2019) and transport and abundance of atmospheric precipitable water (e.g., Suzuki et al., 2013; Wille et al., 2019). In conjunction with increasing understanding of shelf basal melting and its time variability (Adusumilli et al., 2020)

600 and understanding the disposition of surface meltwater either within the structure of Antarctic ice shelves or as runoff (e.g., Bell et al. 2017), it is reasonable to anticipate a quantitative assessment of ice shelf resilience in a warming climate.

Data Availability

ERA5 data were obtained as provided by ECMWF, using the Copernicus Climate Change Service (C3S) Climate Data Store. NASA CERES SYN1deg data were obtained from NASA Langley Research Center CERES Data Products archive.

605 MEaSUREs EASE-Grid 2.0 data were obtained from NSIDC. AWS and Field Camp Observations are archived at the University of Wisconsin Antarctic Meteorological Research Center.

Author Contribution

MG performed the data analysis and interpretation as part of her Master of Science thesis at the Scripps Institution of Oceanography. RS provided synoptic and local scale meteorological analysis. AV provided the AWARE surface energy

610 balance data analysis and contributed to manuscript preparation. JL provided interpretation of the surface energy balance in the case studies and contributed to manuscript preparation. ML provided the AWS and field camp data and their interpretation for this work. DL served as thesis advisor for MG and contributed to manuscript preparation.

Acknowledgments

615 MG and DL were supported by NSF Grant OPP-1744954 and US Department of Energy Grant DE-SC0017981. AV was supported by DOE ASR under contract DE-SC0012704. JL was supported by the National Aeronautics and Space Administration under grant 80NSSC18K1025. ML was supported by NSF Grant OPP-1924730. We thank Dr. Walt Meier of NSIDC for assistance with the MEaSUREs EASE-Grid 2.0 data.

References

620 Adusumilli, S., Fricker, H. A., Medley, B., Padman, L., and Siegfried, M. R.: Interannual variations in meltwater input to the Southern Ocean from Antarctic ice shelves, Nat. Geosci., doi:10.1038/s-41561-020-0616-a, 2020.

Alley, R. B., Anandakrishnan, S., Christianson, K., Horgan, H. J., Muto, A., Parizek, B. R., Pollard, D., and Walker, R. T.: Oceanic forcing of ice-sheet retreat: West Antarctica and more, Ann. Rev. Earth Planet. Sci., 43, 207-231, doi:10.1146/annurev-earth-060614-105344, 2015.

625 Bell, R. E., Chu, W., Kingslake, J., Das, I., Tedesco, M., Tinto, K. J. and Coauthors, Antarctic ice shelf potentially stabilized by export of meltwater in surface river, Nature, 544, 344-351, doi:10.1038/nature22048, 2017.

Bell, R. E., Banwell, A. F., Trusel, L. D., and Kingslake, J.: Antarctic surface hydrology and impacts on ice-sheet mass balance, Nat. Clim. Change, 8, 1044-1052, doi:10.1038/s41558-018-0326-3, 2018.

Bennartz, R., Shupe, M. D., Turner, D. D., Walden, V. P., Steffen, K., Cox, C. J., Kulie, M. S., Miller, N. B., and Pettersen, 630 C.,: July 2012 Greenland melt extent enhanced by low-level liquid clouds, Nature, 496, 83-86, doi:10.1038/nature12002, 2013.

Brodzik, M. J., Long, D. G., Hardman, M. A., Paget, A., and Armstrong, R.: MEsSUREs Calibrated Enhanced-Resolution Passive Microwave Daily EASE-Grid 2.0 Brightness Temperature ESDR, Version 1. Boulder, Colorado, USA. National Snow and Ice Data Center Distributed Active Archive Center, doi:10.5067/MEASURES/CRYOSPHERE/NSIDC-635 0630.001, 2016, Updated 2020.

Bromwich, D. H., Nicolas, J. P., Monaghan, A. J., Lazzara, M. A., Keller, L. M., Weidner, G. A., and Wilson, A. B.: Central West Antarctica among the most rapidly warming regions on Earth, Nat. Geosci., 6, 139-145, doi:10.1038/NGEO2016, 2013.

Chylek, P., Robinson, S., Dubey, M. K., King, M. D., Fu, Q., and Clodius, W. B.: Comparison of near-infrared and thermal 640 infrared cloud phase detections, J. Geophys. Res., 111, D20203, doi:10.1029/2006JD007140, 2006.

Das, S. B., and Alley, R. B.: Characterization and formation of melt layers in polar snow: Observations and experiments from West Antarctica, J. Glaciol., 51, 307-312, doi:10.3189/172756505781829395,2005.

Das, S. B., and Alley, R. B.: Rise in frequency of surface melting at Siple Dome through the Holocene: Evidence for increasing marine influence on the climate of West Antarctica, J. Geophys. Res., 113(D2), D02112, doi:10.1029/2007JD008790, 2008.

Datta, R. T., Tedesco, M., Fettweis, X., Agosta, C., Lhermite, S., Lenaerts, J. T. M., and Wever, N.: The effect of Foehn-induced surface melt on firn evolution over the northeast Antarctic Peninsula, Geophys. Res. Lett., 46, 3822-3831, doi:10.1029/2018GL080845, 2019.

DeConto, R. M., and Pollard, D.: Contribution of Antarctica to past and future sea-level rise, Nature, 531, 591-597, doi:10.1038/nature17145, 2016.

Dee, D., Uppala, S. M., Simmons, A. J., Berrisford, P., Poli, P., Kobayashi, S., and Coauthors: The ERA-Interim reanalysis: Configuration and performance of the data assimilation system, Q. J. Roy. Meteorol. Soc., 137(656), 553-597, doi:10.1002/qj.828, 2011.

Donat-Magnin, M., Jourdain, N. C., Gallée, H., Amory, C., Kittel, C., Fettweis, X. and Coauthors: Interannual variability of summer surface mass balance and surface melting in the Amundsen sector, West Antarctica, The Cryosphere, 14, 229-249, doi:10.5194/tc-14-229-2020, 2020.

Dreschel, S., and Mayr, G. J.: Objective forecasting of foehn winds for a subgrid-scale alpine valley, Weather and Forecasting, 23, 205-218, doi:10.1175/2007WAF2006021.1, 2008.

Dutra, E., Balsamo, G., Viterbo, P., Miranda, P. M. A., Beljaars, A., Schär, C. and Elder, K.: An improved snow scheme for the ECMWF Land Surface Model: Description and offline validation. J. Hydrometeorol., 11, 899-915, doi:10.1175/2010JHM1249.1, 2010.

Elvidge, A. D., Renfrew, I. A., King, J. C., Orr, A., Lachlan-Cope, T. A., Weeks, M., and Coauthors: Foehn jets over the Larsen C Ice Shelf, Antarctica, Q. J. Roy. Meteorol. Soc., 141, 698-713, doi:10.1002/qj2382, 2015.

Fisher, A. T., Mankoff, K. D., Tulaczyk, S. M., Tyler, S.W., and Foley, N.: High geothermal heat flux measured below the West Antarctic Ice Sheet. Sci. Adv., 1, doi:10.1126/sciadv.1500093, 2015.

Fürst, J. J., Durand, G., Gillet-Chaulet, F., Tavard, L. Ranki, M., Braun, M., and Gagliardini, O.: The safety band of Antarctic ice shelves, Nat. Clim. Change, 6, 479-482, doi:10.1038/NCLIMATE2912, 2016.

Glasser, N. F., and Scambos, T. A.: A structural glaciological analysis of the 2002 Larsen B ice shelf collapse, J. Glaciol., 54, 3-16, 2008.

Haran, T., Bohlander, J., Scambos, T., Painter, T., and Fahnestock, M. MODIS Mosaic of Antarctica 2008-2009 (MOA2009) Image Map. [West Antarctica]. Boulder, Colorado USA: National Snow and Ice Data Center. http://dx.doi.org/10.7265/N5ZK5DM5, 2014.

Hersbach, H., Bell, B., Berrisford, P., Hirahara, S., Horányi, A., Muñoz-Sabater, J., and Coauthors: The ERA5 global reanalysis, Q. J. Roy. Meteorol. Soc., 1-51, doi:10.1002/qj.3803, 2020.

675 Hines, K. J., Bromwich, D. H., Wang, S.-H., Silber, I., Verlinde, J., and Lubin, D.: Microphysics of summer clouds in central West Antarctica simulated by the Polar Weather Research and Forecasting Model (WRF) and the Antarctic Mesoscale Prediction System (AMPS), Atmos. Chem. Phys., 19, 12431-12454, https://doi.org/10.5194/acp-19-12431-2019, 2019.

Joughin, I., Smith, B. E., and Medley, B.: Marine ice sheet collapse potentially under way for the Thwaites Glacier Basin, West Antarctica, Science, 344, 735-738, 2014.

680 King, J. C., Kirchgaessner, A., Bevan, S., Elvidge, A. D., Kuipers Munneke, P., Luckman, A., and Coauthors: The impact of fohn winds on surface energy balance during the 2010-2011 melt season over Larsen C Ice Shelf, Antarctica, J. Geophys. Res., 122, 12062-12076, doi:10.1002/2017/JD026809, 2017.

Kingslake, J., Ely, J. C., Das, I., and Bell, R.: Widespread movement of meltwater onto and across Antarctic ice shelves, Nature, 544, 349-352, doi:10.1038/nature22049, 2017.

685 Kuipers Munneke, P., Picard, G., van den Broeke, M. R., Lenaerts, J. T. M., and van Meijgaard, E.: Insignificant change in Antarctic snowmelt volume since 1979, Geophys. Res. Lett., 39, L01501, doi:10.1029/2011GL050207, 2012.

Lazzara, M. A., Weidner, G. A., Keller, L. M., Thom, J. E., and Cassano, J. J.: Antarctic automatic weather station program: 30 years of polar observations, Bull. Amer. Meteorol. Soc., 93, 1519-1537, doi:10.1175/BAMS-D-11-00015.1, 2012.

Lenaerts, J. T. M., Van Tricht, K., Lhermite, S., and L'Ecuyer, T. S.: Polar clouds and radiation in satellite observations,
690 reanalyses, and climate models, Geophys. Res. Lett., 44, 3355-3364, doi:10.1002/2016GL072242, 2017.

Lenaerts, J. T. M., Ligtenberg, S. R. M., Medley, B., Van De Berg, J. J., Konrad, H., Nicolas, J. P., and Coauthors: Climate and surface mass balance of coastal West Antarctica resolved by regional climate modeling, Ann. Glaciol., 59, 29-41, doi:10.1017/aog.2017.42, 2018.

Lubin, D., Zhang, D., Silber, I., Scott, R. C., Kalogeras, P., Battaglia, A. and Coauthors: AWARE: The Atmospheric Radiation
695 Measurement (ARM) West Antarctic Radiation Experiment, Bull. Amer. Meteorol. Soc., 101 (7): E1069–E1091, doi:10.1175/BAMS-D-18-0278.1, 2020.

Mather, J. H., and Voyles, J. W.: The ARM Climate Research Facility: A review of structure and capabilities, Bull. Amer. Meteorol. Soc., March 2013, 377-392, doi:10.1175/BAMS-D-11-00218.1, 2013.

Mouginot, J., Rignot, E., Bjork, A. A., van den Broeke, M., Millan, R., Morlighem, M., and Coauthors: Forty-six years of
700 Greenland Ice Sheet mass balance from 1972-2018, Proc. Nat. Acad. Sci., 116, 9239-9244, doi:10.1073/pnas.1904242116, 2019.

Nicolas, J. P, and Bromwich, D. H.: Climate of West Antarctica and influence of marine air intrusions, J. Climate., 24, 49-67, doi: 10.1175/2010JCLI3522.1, 2011.

Nicolas, J. P., Vogelmann, A. M., Scott, R. C., Wilson, A. B., Cadeddu, M. P., Bromwich, D. H., and Coauthors: January 2016
705 extensive summer melt in West Antarctica favoured by strong El Niño, Nat. Comms., 8, 15799. doi:10.1038/ncomms15799, 2017.

Oppenheimer, M.: Global warming and the stability of the West Antarctic Ice Sheet. *Nature*, **393**, 325-332, 1998.

Paolo, F. S., Fricker, H. A., and Padman, L.: Volume loss from Antarctic ice shelves is accelerating, Science, 348, 327-330, 2015.

710   Pritchard, H. D., Ligtenberg, S. R. M., Fricker, H. A., Vaughan, D. G., van den Broeke, M. R., and Padman, L.: Antarctic ice-sheet loss driven by basal melting of ice shelves, Nature, 484, 502-505, doi:10.1038/nature10968, 2012.

Rignot, E., Mouginot, J., Scheuchl, B., van den Broeke, M., van Wessem, M. J., and Morlighem M.: Four decades of Antarctic ice sheet mass balance from 1979-2017, Proc. Nat. Acad. Sci., 116, 1095-1103, doi:10.1073/pnas.1812883116, 2019.

Rutan, D. A., Kato, S., Doelling, D. R., Rose, F. G., Nguyen, L. T., Caldwell, T. E., and Loeb N. G.: CERES Synoptic Product:
715   Methodology and validation of surface radiant flux, J. Atmos. Ocean. Tech., 32, 1121-1143, doi:10.1175/JTECH-D-14-00165.1, 2015.

Scambos, T. A., Hulbe, C., and Fahnestock, M.: Climate-induced ice shelf disintegration in the Antarctic Peninsula, AGU Antarct. Res. Ser., 79, 79-92, 2003.

Scambos, T. A., Bohlander, J. A., Shuman, C. A., and Skvarca, P.: Glacier acceleration and thinning after ice shelf collapse in
720   the Larsen B embayment, Antarctica, Geophys. Res. Lett., 31, L18402, doi:10.1029/2004GL020670, 2004.

Scambos, T. A., Haran, T., Fahnestock, M., Painter, T., and Bohlander, J.: MODIS-based Mosaic of Antarctica (MOA) data sets: Continent-wide surface morphology and snow grain size, Rem. Sens. Environ., 111, 242-257, doi:10.1016/j.rse.2006.12.020, 2007.

Scambos, T. A., Fricker, H. A., Liu, C.-C., Bohlander, J., Fastook, J., Sargent, A., Massom, R., and Wu, A.-M.: Ice shelf
725   disintegration by plate bending and hydro-fracture: Satellite observations and model results of the 2008 Wilkins ice shelf break-ups, Earth Planet. Sci. Lett., 280, 51-60, 2009.

Scott, R. C., Lubin, D., Vogelmann, A. M., and Kato, S.: West Antarctic Ice Sheet clouds and radiation budget from NASA A-Train satellites, J. Climate, 30, 6151-6170, doi:10.1175/JCLI-D-16-0644.1, 2017.

Scott, R. C., Nicolas, J. P., Bromwich, D. H., Norris, J. R., and Lubin, D.: Meteorological drivers and large-scale climate
730   forcing of West Antarctic surface melt, J. Climate, 32, 665-684, doi:10.1175/JCLI-D-18-0233.1, 2019.

Silber, I., Verlinde, J., Wang, S.-H., Bromwich, D. H., Fridlind, A. M., Cadeddu, M., and Coauthors: Cloud influence on ERA5 and AMPS surface downwelling longwave radiation biases in West Antarctica, J. Climate, 32, 7935-7949, doi:10.1175/JCLI-D-19-0149.1, 2019.

Steig, E. J., Schneider, D. P., Rutherford, S. D., Mann, M. E., Comiso, J. C., and Shindell, D. T.: Warming of the Antarctic
735   ice-sheet surface since the 1957 International Geophysical Year, Nature, 457, 459-462, doi:10.1038/nature07669, 2009.

Suzuki, K., Yamanouchi, T., Kawamura, K., and Motoyama, H.: The spatial and seasonal distributions of air-transport origins to the Antarctic based on 5-day backward trajectory analysis, Polar Sci., 7, 205-213, doi:10.1016j.polar.2013.08.001, 2013.

Tedesco, M.: Assessment and development of snowmelt retrieval algorithms over Antarctica from K-band spaceborne
740   brightness temperature (1979-2008), Rem. Sens. Environ., 113, 979-997, 2009.

Torinesi, O., Fily, M., and Genthon, C.: Variability and trends of the summer melt period of Antarctic ice margins since 1980 from microwave sensors. J. Climate, 16, 1047-1060, 2003.

Trusel, L. D., Frey, K. E., Das, S. B., Kuipers Munneke, P., and van den Broeke, M. R.: Satellite-based estimates of Antarctic surface meltwater fluxes, Geophys. Res. Lett., 40(23), 6148-6153, doi:10.1002/2013GL058138, 2013.

745 van den Broeke, M.: Strong surface melting preceded collapse of Antarctic Peninsula ice shelf, Geophys. Res. Lett., 32, L12815, doi:10.1029/2005GL023247, 2005.

Van Tricht, K., Lhermite, S., Lenaerts, J. T. M., Gorodetskaya, I. V., L'Ecuyer, T. S., Noël, B., and Coauthors: Clouds enhance Greenland Ice Sheet meltwater runoff, Nat. Comms., 7, 10266, doi:10.1038/ncomms10266, 2016.

Weertman, J.: Stability of the junction of an ice sheet and an ice shelf, J. Glaciol., 13, 3-11, 1974.

750 Wille, J. D., Favier, V., Dufour, A., Gorodetskaya, I. V., Turner, J., Agosta, C., and Codron, F.: West Antarctic surface melt triggered by atmospheric rivers, Nat. Geosci., 12, 911-916, doi:10.1038/s41561-019-0460-1, 2019.

Zhou, X., Bromwich, D. H., Nicolas, J. P., Montenegro, A., and Wang, S.-H.: West Antarctic surface melt event of January 2016 facilitated by föhn warming, Q. J. Roy. Meteorol. Soc., 145, 687-704, doi:10.1002/qj3460, 2018.

Zwally, H. J., and Feigles, S.: Extent and duration of Antarctic surface melting. J. Glaciol., 40, 463-476, 1994.